Monthly Notices
of the
ROYAL ASTRONOMICAL SOCIETY

MNRAS **516,** 2389–2405 (2022)
Advance Access publication 2022 July 29

https://doi.org/10.1093/mnras/stac2069

Shapes of Milky-Way-mass galaxies with self-interacting dark matter

Drona Vargya,[1★] Robyn Sanderson,[1,2] Omid Sameie,[3] Michael Boylan-Kolchin,[3] Philip F. Hopkins,[4] Andrew Wetzel[5] and Andrew Graus[3]

[1]*Department of Physics and Astronomy, University of Pennsylvania, 209 South 33rd Street, Philadelphia, PA 19104, USA*
[2]*Center for Computational Astrophysics, Flatiron Institute, 162 Fifth Avenue, New York, NY 10010, USA*
[3]*Department of Astronomy, The University of Texas at Austin, 2515 Speedway, Stop C1400, Austin, TX 78712, USA*
[4]*TAPIR, California Institute of Technology, MC 350-17, Pasadena, CA 91125, USA*
[5]*Department of Physics and Astronomy, University of California, Davis, One Shields Avenue, Davis, CA 95616, USA*

Accepted 2022 July 12. Received 2022 June 20; in original form 2021 April 29

ABSTRACT

Self-interacting dark matter (SIDM) models offer one way to reconcile inconsistencies between observations and predictions from collisionless cold dark matter (CDM) models on dwarf-galaxy scales. In order to incorporate the effects of both baryonic and SIDM interactions, we study a suite of cosmological-baryonic simulations of Milky-Way (MW)-mass galaxies from the Feedback in Realistic Environments (FIRE-2) project where we vary the SIDM self-interaction cross-section σ/m. We compare the shape of the main dark matter (DM) halo at redshift $z = 0$ predicted by SIDM simulations (at $\sigma/m = 0.1$, 1, and 10 $\mathrm{cm^2\,g^{-1}}$) with CDM simulations using the same initial conditions. In the presence of baryonic feedback effects, we find that SIDM models do not produce the large differences in the inner structure of MW-mass galaxies predicted by SIDM-only models. However, we do find that the radius where the shape of the total mass distribution begins to differ from that of the stellar mass distribution *is* dependent on σ/m. This transition could potentially be used to set limits on the SIDM cross-section in the MW.

Key words: methods: numerical – galaxies: haloes – galaxies: structure – dark matter.

1 INTRODUCTION

The cold dark matter (CDM) plus dark energy (ΛCDM) cosmological model has been the most successful model for understanding the large-scale structure of the Universe. However, on length scales smaller than ~1 Mpc and masses smaller than $\sim 10^{11}$ $\mathrm{M_{\odot}}$, there are challenges to this model from discrepancies between predictions from CDM-only simulations and observational data. On dwarf galaxy ($M_{\star} \lesssim 10^9$ $\mathrm{M_{\odot}}$) scales, these discrepancies include the core-cusp, diversity, missing satellites, too-big-to-fail (TBFT), and planes-of-satellites 'problems' (Bullock & Boylan-Kolchin 2017; Tulin & Yu 2018, and references therein). The *core-cusp* problem (Moore 1994; Kuzio de Naray, McGaugh & de Blok 2008; Oh et al. 2008; Walker & Peñarrubia 2011; Oh et al. 2015) arises from observational evidence that the cores of dark matter (DM) dominated galaxies are less dense and less cuspy (in inner density profile slope) than predicted by CDM-only simulations. The *diversity* problem, both in the field and among the Milky Way's (MW) satellites (Oman et al. 2015; Kaplinghat, Valli & Yu 2019), arises from observational evidence that galaxies' rotation curves appear to be more varied than in CDM simulations. The *missing satellites* problem (Klypin et al. 1999; Moore et al. 1999) refers to the smaller number of observed satellite (dwarf) galaxies around the MW and the Local Group than the number of subhaloes predicted by CDM-only simulations. The *too-big-to-fail* problem (Boylan-Kolchin, Bullock & Kaplinghat 2011, 2012; Garrison-Kimmel et al. 2014) arises from a mismatch in the central densities of satellite and field galaxies, which are smaller than predicted by CDM-only simulations; it is expected that haloes so massive are resistant to star formation suppression from re-ionization (thus 'too big to fail' in forming stars). Finally, the *planes-of-satellites* phenomenon refers to the apparent alignment of the orbital planes of satellite galaxies in the MW (e.g. Lynden-Bell 1976; Kroupa, Theis & Boily 2005; Pawlowski, Pflamm-Altenburg & Kroupa 2012; Fritz et al. 2018; Pawlowski & Kroupa 2020; though see also Riley & Strigari 2020), M31 (e.g. Conn et al. 2013; Ibata et al. 2013), and Centaurus A (Müller et al. 2018), which is not commonly seen in CDM-only simulations (e.g. Libeskind et al. 2009; Ibata et al. 2014); however, transient coplanar configurations are seen when baryons are included (e.g. Ahmed, Brooks & Christensen 2017; Shao, Cautun & Frenk 2019; Samuel et al. 2021).

In order to solve these challenges on small scales without affecting large-scale structure, solutions within the CDM framework have been proposed to reconcile observations with predictions through a more complete incorporation of the baryonic physics (Navarro, Frenk & White 1996; Mashchenko, Wadsley & Couchman 2008; Governato et al. 2012; Peñarrubia et al. 2012; Pontzen & Governato 2012; Brooks & Zolotov 2014; Oñorbe et al. 2015). Alternatively, the aforementioned discrepancies may hint toward a theory of DM beyond the CDM model.

Self-interacting dark matter (SIDM) models (Spergel & Steinhardt 2000) assume DM particles can exchange energy and momentum via a force mediator with a cross-section close to the regime of the strong interaction (Ahn & Shapiro 2005; Ackerman et al. 2009; Arkani-Hamed et al. 2009; Feng et al. 2009; Loeb & Weiner 2011; Tulin, Yu & Zurek 2013). On galactic scales, the DM interaction

---

★ E-mail: vad@sas.upenn.edu

Published by Oxford University Press on behalf of Royal Astronomical Society

rate becomes comparable to Hubble time-scale only deep inside of the gravitational potential, leaving the outer radii and extragalactic scales intact (Rocha et al. 2013; Vogelsberger et al. 2016; Sameie et al. 2019; Bondarenko et al. 2021). In the inner regions of DM-dominated systems, energy-exchange through self-interactions will result in an isothermal density profile if the SIDM local collision rate $\Gamma_{\rm scatter} \propto \rho_{\rm DM}\, \sigma_{\rm x}/m_{\rm x} \geq 1$, where $\rho_{\rm DM}$ is the DM density and $\sigma_{\rm x}/m_{\rm x}$ is the self-interaction cross-section per unit mass. The value of $\sigma_{\rm x}/m_{\rm x}$ is constrained by observations of galaxy clusters (Yoshida et al. 2000; Randall et al. 2008; Peter et al. 2013) and of the internal stellar kinematics of MW satellites (Koda & Shapiro 2011; Zavala, Vogelsberger & Walker 2013; Valli & Yu 2018; Correa 2021; Hayashi et al. 2021).

Cosmological DM-only simulations of SIDM models have made baseline predictions for their velocity profiles, density profiles, halo shapes, and substructures (Vogelsberger, Zavala & Loeb 2012; Peter et al. 2013 ; Rocha et al. 2013). These simulations predict isothermal density profiles and spherical shapes for DM haloes and their substructures. Introducing baryonic components in SIDM haloes couples the central DM densities to the baryonic potential (Kaplinghat et al. 2014; Elbert et al. 2018; Sameie et al. 2018), leading to substantial differences from DM-only predictions when baryons are dynamically important. This suggests that a plausible explanation of the observed diversity in the DM distribution in field galaxies and the MW's satellites could be that it is a byproduct of baryonic mass assembly and DM self-interactions (Creasey et al. 2017; Kamada et al. 2017; Despali et al. 2019; Ren et al. 2019; Sameie et al. 2020b, a).

DM self-interactions also lead to more spherical halo shapes in SIDM than CDM (Peter et al. 2013). Cosmological mass assembly in CDM creates triaxial DM haloes: since angular momentum exchange is inefficient, the DM particles retain substantial memory of their initial in-fall directions, resulting in haloes with ellipsoidal minor-to-major axis ratios as low as $c/a \sim 0.5$ (Vera-Ciro et al. 2011; Butsky et al. 2016). In pure SIDM, particles can more efficiently exchange angular momentum through interactions, isotropizing their orbits until $c/a \sim 1$. However, if baryons dominate the gravitational potential, DM self-interactions tie the DM halo shapes to the baryonic distribution. Semi-analytic modeling suggests that the SIDM density profile should scale with the *total* gravitational potential (Kaplinghat et al. 2014). If baryons dominate the central density of galaxies, the shape of the SIDM distribution should then follow that of the baryons. *N*-body SIDM simulations of MW-mass systems with embedded baryonic discs support these predictions (Sameie et al. 2018), as do the SIDM cosmological-baryonic simulations of slightly more massive disc galaxies (at $z \sim 0.2$) by Despali et al. (2019).

In this work and a companion paper (Sameie et al. 2021), we examine high-resolution cosmological-baryonic simulations of MW-mass galaxies from the 'Feedback In Realistic Environments' (FIRE) project. The initial conditions and CDM simulations are part of the second generation of simulations, the FIRE-2 suite (Hopkins et al. 2018); we also study the same initial conditions resimulated with several different SIDM cross-sections. As in the original FIRE-2 suite, gravity and hydrodynamics are solved with `GIZMO` and baryonic feedback is implemented with the FIRE-2 feedback recipes, which are held constant across all runs (for exact details, see Sameie et al. 2021, and Section 3 of this paper). Simulations with SIDM use the Monte Carlo approach to scattering described in Rocha et al. (2013). We also resimulate some haloes without baryons, in both CDM and SIDM, to isolate feedback effects. Our goal in this work is to gauge the extent to which halo shapes can serve as a discriminator between CDM and SIDM and the extent to which this depends on the self-consistent inclusion of baryonic physics.

The CDM cosmological-baryonic versions of these simulations have previously been shown to produce a realistic population of satellite galaxies around MW-mass hosts that does not suffer from the *missing satellites* or *TBFT* problems of small-scale structure formation (Wetzel et al. 2016; Garrison-Kimmel et al. 2019; Samuel et al. 2020, 2021). Furthermore, studies across mass scales have shown that the *core-cusp* (Chan et al. 2015; Oñorbe et al. 2015; El-Badry et al. 2016) and *diversity* (El-Badry et al. 2018) problems are also mitigated with this feedback implementation. Other groups find similar results with different physics implementations (e.g. Brooks et al. 2013; Brooks & Zolotov 2014; Dutton et al. 2016; Tollet et al. 2016). Since baryonic physics can thus at least partially reconcile observations with the standard ΛCDM cosmological model, we must also carefully gauge whether SIDM, combined with baryonic feedback, *over*-corrects the potential small-scale problems for ΛCDM.

This work is organized as follows. In Section 2, we outline the method used to determine the shapes of haloes. In Section 3, we detail the suite of simulations used in this study. In Section 4, we compare the results for the densities, velocities, scattering rates, shapes, and triaxiality between FIRE-2 MW-mass CDM and SIDM with previous results from simulations and observations. In Section 5, we discuss the results. In Section 6, we give a summary of our results and conclusions.

2 METHODS OF DETERMINING SHAPES

To determine halo shapes, we use the iterative algorithm introduced in Dubinski & Carlberg (1991; also see Allgood et al. 2006; Vera-Ciro et al. 2011; Bullock & Boylan-Kolchin 2017; Sameie et al. 2018; Robertson et al. 2019). This procedure fits a triaxial ellipsoid to the approximate isodensity surface of particles starting from a series of spherical radii $\{r\}$ from the galactic-centre by determining the weighted inertia tensor for particles inside each r. We determine the axis ratios of these ellipsoids for each separate species in the simulations (DM, stars, and gas) and for the total mass distribution (which includes all particles from each species). The axis lengths of the ellipsoids are labelled as $a(r) \geq b(r) \geq c(r)$, where $a(r)$, $b(r)$, and $c(r)$ are lengths of the major, intermediate, and minor semi-axes, respectively. The axis lengths are defined as functions of r to allow for changing shapes at different radii. The axis ratios are then defined as

$$s(r) \equiv \frac{c(r)}{a(r)}\,, \quad p(r) \equiv \frac{c(r)}{b(r)}\,, \quad q(r) \equiv \frac{b(r)}{a(r)}\,. \tag{1}$$

We begin the iterative algorithm by calculating the weighted (or 'reduced') inertia tensor, which is a symmetric matrix defined as

$$\tilde{I}_{ij}(r) = \sum_{n=1}^{N_c} \frac{m_n\, x_{i,n}\, x_{j,n}}{d_n^2(r)} \Bigg/ \sum_{n=1}^{N_c} m_n\,, \quad i, j \in \{1, 2, 3\}\,, \tag{2}$$

where N_c is the number of particles within the ellipsoid of each component (or species), m_n is the nth particle mass, and $x_{i,\,n}$ is the ith coordinate of the nth particle for each component with respect to a Cartesian coordinate system. In our final, best-fitting ellipsoid coordinate system, x_1 (x_2, x_3) corresponds to the distance along the major (intermediate, minor) axis. The tensor is 'reduced' by normalizing the particle positions $\{x\}$ by the ellipsoidal distance

$d_n(r)$[1] (which is measured in the eigenvector coordinate system from the centre to the nth particle), where

$$d_n^2(r) = x_{1,n}^2 + \frac{x_{2,n}^2}{q^2(r)} + \frac{x_{3,n}^2}{s^2(r)} \,. \tag{3}$$

We then find the three eigenvalues ($\lambda_1 \geq \lambda_2 \geq \lambda_3$) of the matrix $\tilde{I}_{ij}$ and set the ellipsoidal orientation to the corresponding orthogonal eigenvectors $\{\mathbf{e_1}, \mathbf{e_2}, \mathbf{e_3}\}$ (i.e. the principal axes). The square roots of the eigenvalues are used to find the axis ratios: $s = (\lambda_3/\lambda_1)^{1/2}$, $p = (\lambda_3/\lambda_2)^{1/2}$, and $q = (\lambda_2/\lambda_1)^{1/2}$. The axis lengths are then computed with these axis ratios: $a(r) = r$, $b(r) = r\,q(r)$, and $c(r) = r\,s(r)$. This ensures that the triaxial ellipsoid is contiguous to the bounding sphere of radius r at two points.

For every r, the ellipsoid is initialized as a sphere, i.e. $s(r) = p(r) = q(r) = 1$, and the inertia matrix, eigenvalues, and eigenvectors are computed. In the second (and every subsequent) iteration, the inertia matrix is recomputed using particles that fall inside the reshaped and reoriented ellipsoid from the previous iteration. This method keeps the largest axis length $a(r)$ constant, and thus, constrains this semimajor axis of the ellipsoid to lie on the surface of the bounding sphere. Therefore, particles are added and removed to the set only within spherical radius r. We continue the iterations until either $\Delta s = |s_k - s_{k-1}|$, $\Delta p = |p_k - p_{k-1}|$, and $\Delta q = |q_k - q_{k-1}|$ are all $<10^{-3}$, or until a maximum of $k = 1000$ iterations.

3 SIMULATIONS OF MW-MASS GALAXIES

This work compares different resimulations of three zoomed-in, cosmological-baryonic simulations of MW-mass haloes from the Latte suite of FIRE-2 simulations (see Hopkins et al. 2018). The initial conditions for the haloes are all drawn from the same low-resolution cosmological box (AGORA; Kim et al. 2014) and are labelled `m12f`, `m12i`, and `m12m`. The size of the zoomed-in region varies between 2–5 Mpc, depending on the formation history of each halo. The haloes are selected to have present-day virial masses between $1.2–1.6 \times 10^{12}$ M$_\odot$, similar to that of the MW, and to have no massive companions within at least $5R_{200\mathrm{m}} \sim 1.5$ Mpc.[2]

The full FIRE-2 suite of 18 cosmological-baryonic zooms that have been run at this mass scale includes simulations that form thin discs similar to the MW's, as well as some that form spheroids (El-Badry et al. 2018; Garrison-Kimmel et al. 2018). We select these particular three systems for resimulation because the properties of their CDM versions have been extensively compared to the MW. Their disc structure (Sanderson et al. 2020), their satellite galaxy systems (Samuel et al. 2021), and their stellar haloes (Sanderson et al. 2018) all have reasonable similarity to the MW. These are not the only three systems within the suite for which this is true, but they are the ones for which the similarities and differences have been most thoroughly quantified. As in the CDM versions, we use an initial mass resolution of 7100 M$_\odot$ for the star and gas particles, and 35 000 M$_\odot$ for DM particles, for all resimulations.

The primary difference between the three haloes chosen for resimulation is their formation histories. `m12m` forms earliest and has the largest disc scale radius of the three (Debattista et al. 2019). `m12f` forms latest and includes a late interaction with a Small Magellanic Cloud (SMC)-mass galaxy that disrupts the disc (Sanderson et al. 2018). `m12i` has an intermediate formation epoch, the largest proportion of accretion from low-mass satellites, and a thicker, younger disc with a significant outer warp (Wetzel et al. 2016; Sanderson et al. 2020).

We compare resimulations of these three haloes with the following set of variations at redshift $z = 0$, summarized in Table 1:

(i) **CDM-only – Collisionless CDM without baryons**, for all three haloes;

(ii) **SIDM-only – Collisional self-interacting DM without baryons**, at $\sigma/m = 1$ and 10 cm^2 g^{-1} for `m12f`;

(iii) **CDM+Baryon – Collisionless CDM with baryons and full hydrodynamics**, using FIRE-2 feedback recipes, for all three haloes;

(iv) **SIDM+Baryon – Collisional self-interacting DM with baryons and full hydrodynamics**, with identical baryonic physics to the fiducial suite, at $\sigma/m = 0.1$ cm^2 g^{-1} for `m12m`, and 1 and 10 cm^2 g^{-1} for all three haloes, but at redshift $z = 0.1$ ($t = 12.5$ Gyr) for `m12i` at the latter cross-section.

All DM self-interactions are realized using Monte Carlo elastic (non-dissipative) scattering, as described in Rocha et al. (2013). We evaluate the `m12i` SIDM+Baryon $\sigma/m = 10$ cm^2 g^{-1} at $z = 0.1$, the latest epoch currently available for this resimulation. Based on the behaviour observed in the other runs, we expect the radial density and velocity profile of this simulated galaxy to be relatively stable between $z = 0.1$ and $z = 0$. The shape profiles of the various species continue to evolve to $z = 0$ in the central parts of the galaxies, but this effect is least pronounced for the DM component.

The baryonic runs listed above and in Table 1 use the standard set of FIRE-2 feedback recipes (Hopkins et al. 2018) with one exception, which is to ignore the conversion of thermal to kinetic energy in the unresolved Sedov–Taylor phase of the expansion of shocks generated by mass loss from massive stars. As discussed in Sameie et al. (2021), the default prescription in FIRE-2 had the effect of converting nearly all the thermal energy into momentum, giving the stellar winds a similar effect to a miniature supernova and resulting (perhaps counter-intuitively) in higher star formation rate (SFR) and stellar mass in the simulated galaxies, and subsequently less diversity among density profiles. However, for this study we use the resimulations of the CDM haloes that ignore this '*PdV*' work for the sub-res regions, for consistency with the existing SIDM runs.

Fig. 1 shows spectral energy distribution (SED)-modeled and ray-traced images (integrated over filter band-passes similar to *Hubble Space Telescope* visible light) of the simulated galaxies in a wide-angle view focused on the stellar halo. It is apparent that although there are some small differences, every simulation contains a reasonable-looking spiral galaxy, system of dwarf satellite galaxies, and stellar halo. One obvious difference between resimulations of the same initial conditions is in the particular dwarf satellites that appear in each simulation, which vary between even identical runs due to the stochastic impact of supernovae. The most massive satellites are stable to this effect but can have small phase differences in their orbits from run to run, as is evident in `m12f`. The other obvious difference is in the star formation rate (as evident in `m12i`). Star formation is a highly non-linear process, and also varies stochastically from run to run even for identical initial conditions, again mainly because of the random occurrence and clustering of supernovae and also (as clearly seen in `m12f`) from differences in the orbital phase of mergers. However, these differences do not significantly change the global properties of the haloes and their central galaxies, as we next demonstrate.

---

[1] The unweighted inertia tensor $I_{ij}(r)$ (without the tilde), does not 'reduce' the matrix with the ellipsoidal normalization distance measure $d_n(r)$.

[2] $R_{200\mathrm{m}}$ is the radius within which the total mass density, $\bar{\rho} \equiv 3M(<R_{200\mathrm{m}})/4\pi R_{200\mathrm{m}}^3$, is 200 times the average matter density.

Table 1. Summary of simulated MW-mass galaxy properties. All simulations have baryonic particle mass ∼7100 $\mathrm{M}_\odot$ and DM particle mass 35 000 $\mathrm{M}_\odot$. An interaction cross-section of $\sigma/m = 0$ $\mathrm{cm}^2\,\mathrm{g}^{-1}$ indicates standard collisionless CDM. $M_{\rm vir}$, $r_{\rm vir}$: Bryan & Norman (1998) spherical virial quantities. r_{-2}: spherical radius where log-slope of DM density profile is −2. d_1: scattering radius, determined as shown in Fig. 7 (Section 4.1); DNI indicates that $\Gamma_{\rm scatter} < t^{-1}_{z=0}$ for all d with sufficient particles to determine $\rho_{\rm DM}(d)$ and $v_{\rm rel}(d) \approx 1.3\, v_{\rm rms}(d)$ (see Fig. 7); that is, the scattering rate profile 'does not intersect' this characteristic value, so d_1 is undefined. $M_{\star,\,90}$, $r_{\star,\,90}$: mass and spherical radius of 90 per cent of stellar mass within 30 kpc of the central galaxy.

Initial conditions	σ/m [$\mathrm{cm}^2\,\mathrm{g}^{-1}$]	$M_{\rm vir}$ [$10^{12}\,\mathrm{M}_\odot$]	$r_{\rm vir}$ [kpc]	r_{-2} [kpc]	d_1 † [kpc]	$M_{\star,\,90}$ [$10^{10}\,\mathrm{M}_\odot$]	$r_{\star,\,90}$ [kpc]	Reference
CDM-only								
`m12f`	0	1.28	284.2	64.6	–	–	–	Garrison-Kimmel et al. (2017)
`m12i`	0	0.90	252.8	24.5	–	–	–	Wetzel et al. (2016)
`m12m`	0	1.14	273.9	35.5	–	–	–	Garrison-Kimmel et al. (2019)
SIDM-only								
`m12f`	1	1.28	284.0	38.9	DNI	–	–	Sameie et al. (2021)
`m12f`	10	1.25	282.0	28.2	24.	–	–	Sameie et al. (2021)
CDM+Baryon								
`m12f`	0	1.33	287.9	19.5	–	5.3	12.4	Garrison-Kimmel et al. (2017)
`m12i`	0	0.96	258.4	17.0	–	3.2	16.7	Wetzel et al. (2016)
`m12m`	0	1.23	280.8	18.6	–	4.9	21.2	Hopkins et al. (2018)
SIDM+Baryon								
`m12m`	0.1	1.22	279.9	17.0	DNI	6.1	23.0	Sameie et al. (2021)
`m12f`	1	1.36	289.8	13.5	8.8	6.2	15.7	Sameie et al. (2021)
`m12i`	1	0.98	260.0	10.7	7.4	5.0	13.9	Sameie et al. (2021)
`m12m`	1	1.24	281.5	9.8	9.8	6.6	20.2	Sameie et al. (2021)
`m12f`	10	1.27	283.2	28.2	23.	5.1	15.9	Sameie et al. (2021)
`m12i` ‡	10	0.92	237.8	24.5	19.	4.5	12.3	Sameie et al. (2021)
`m12m`	10	1.22	279.6	5.4	22.	8.0	20.4	Sameie et al. (2021)

†: d_1 is determined using ellipsoidally averaged DM local collision rate profiles from ellipsoidally averaged density and velocity profiles; all other quantities in this table are determined with spherical averaging. ‡: Values for all simulations are taken at redshift $z = 0$ except for `m12i` SIDM+Baryon $\sigma/m = 10$ $\mathrm{cm}^2\,\mathrm{g}^{-1}$, which is evaluated at $z = 0.1$.

Fig. 2 also shows SED-modeled and ray-traced images, but with close-up views of the stellar discs in the simulated systems. There is remarkable uniformity in the structure and size of the discs across all DM simulations. The `m12f` SIDM simulation has a slightly higher SFR in its outskirts, probably due to the timing of a merger with a roughly ∼SMC-mass object visible in Fig. 1, while `m12i` and `m12m` have no noticeable increase in star formation with σ/m. Generally, the discs of the CDM galaxies tend to be slightly more massive and compact than in SIDM.

Fig. 3 summarizes the characteristic masses and radii of the resimulations, quantifying the impressions given by examining Figs 1 and 2. The left-hand panel shows the DM virial mass $M_{\rm vir}$ versus DM scale radius r_{-2}; the right-hand panel shows the stellar-to-halo mass ratio $M_{\star,\,90}/M_{\rm vir}$ versus the radius enclosing 90 per cent of the stellar mass $r_{\star,\,90}$. These values are all computed using spherical volumes. $M_{\rm vir}$ values are roughly the same over scattered domains of r_{-2} for each set of simulations, while the $M_{\star,\,90}/M_{\rm vir}$ ratios are generally more scattered over $r_{\star,\,90}$. The CDM-only and SIDM-only simulations have larger r_{-2} than their CDM+Baryon and SIDM+Baryon counterparts due to the increased concentration produced by the central baryonic component. For CDM+Baryon and SIDM+Baryon, the `m12f` and `m12i` simulations have the smallest and largest $M_{\rm vir}$, respectively, while the `m12m` simulations fall in-between. The interaction cross-section does not otherwise seem to produce any clear trends in the global DM distribution; `m12m`'s scale radius decreases as σ/m increases, while `m12f` and `m12i` show no clear trend. In all cases the virial mass varies by less than 10 per cent across all cross-sections. Finally, steady growth in $M_{\rm vir}$ and $M_{\star,\,90}$ for `m12i` at 10 $\mathrm{cm}^2\,\mathrm{g}^{-1}$ from 0.1 (plotted) to $z = 0$ (all other runs) would bring this halo into consistency with the other `m12i` simulations, as would further contraction of the DM distribution due to the baryonic component (leading to a decrease in r_{-2}).

In terms of the stellar distributions, there is significant variation in the stellar-to-halo mass ratio across the different resimulations, while $r_{\star,\,90}$ appears roughly independent of σ/m for most cases (although $r_{\star,\,50}$ does have a trend with cross-section; see Sameie et al. 2021). Again `m12m` shows the opposite trend from `m12i` and `m12f`, as well as the largest variation in $M_{\star,\,90}/M_{\rm vir}$. While in `m12f` and `m12i` $M_{\star,\,90}/M_{\rm vir}$ shows no trend for larger σ/m, for `m12m` a larger σ/m gives rise to a relatively more massive central galaxy (recall that the DM halo does not change appreciably in mass between runs).

4 RESULTS

In this section, we compare the density, velocity, and shape profiles of the different simulations described in Section 3. Throughout the rest of this work and the Appendix, we use the same series of line-styles to denote different DM cross-sections, different colours to show the different species, and gradient shaded areas to indicate the SIDM local collision regions (LCR) for different σ/m; these are given in Fig. 4 and apply to all subsequent Figs.

4.1 Densities, velocities, and scattering rates

Predictions for density and velocity distributions in SIDM are closely related to those for the halo's shape, since the same interactions that heat the inner regions also make the outer halo more spherical, by preferentially scattering DM particles on plunging, radial orbits. Before discussing the shapes, we will review the density and velocity profiles for DM (discussed in full in Sameie et al. 2021) and discuss the profiles for the stellar and gas components as well. While Sameie et al. (2021) presents spherically averaged profiles, here we show profiles computed using ellipsoids fit to isodensity contours for each

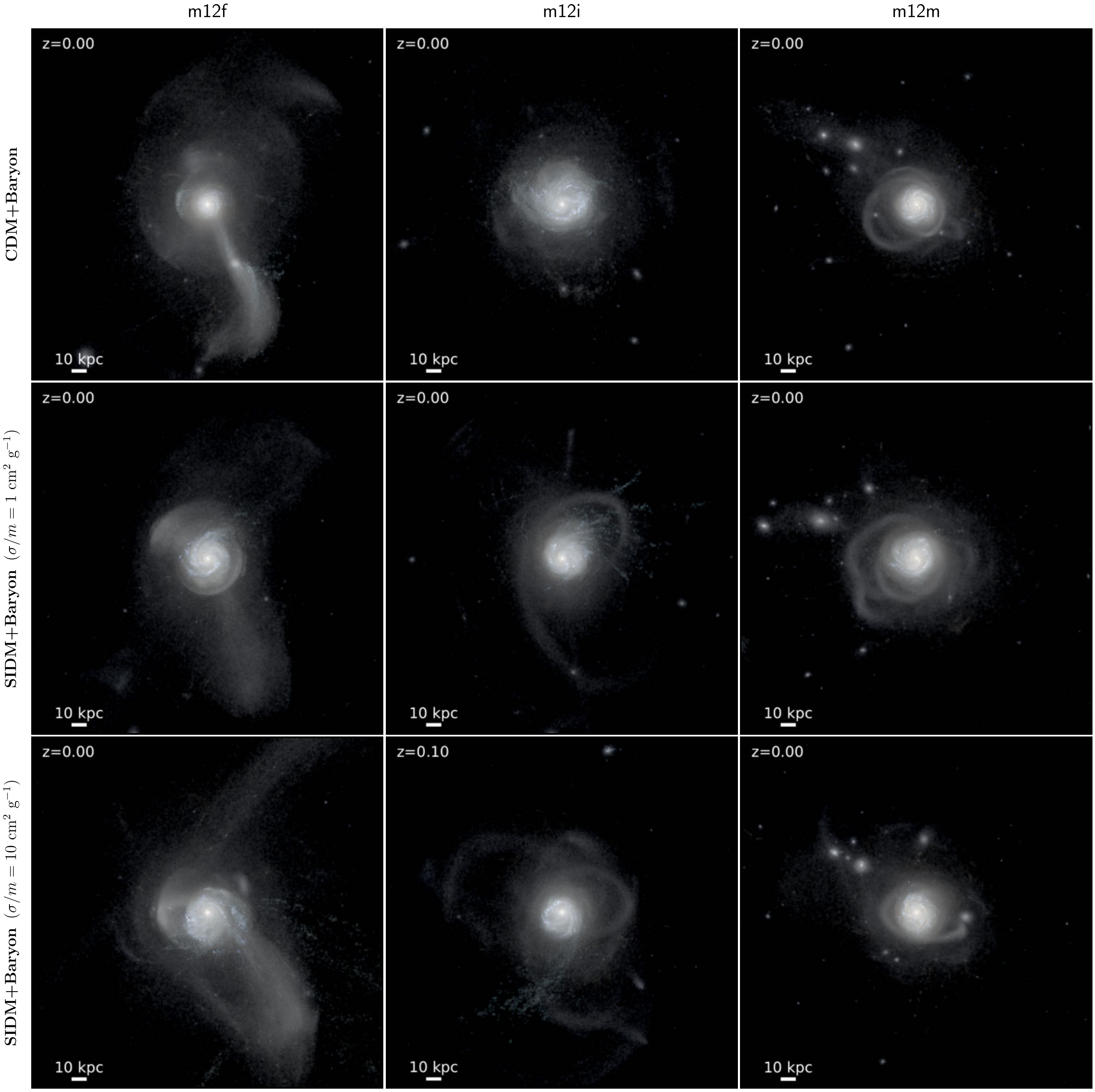

Figure 1. Face-on halo view of cosmological-baryonic simulated MW-mass galaxies. SED-modeled, ray-traced images of starlight in three sets of MW-mass galaxy simulations: `m12f` (left), `m12i` (centre), and `m12m` (right); all DM+Baryon simulations are shown except `m12m` SIDM+Baryon $\sigma/m = 0.1\ \mathrm{cm^2\ g^{-1}}$ (which is quite similar to the `m12m` CDM+Baryon case). Each panel is 300 kpc across and the galaxy has been rotated to show the disc face-on. All simulations except `m12i` SIDM+Baryon $\sigma/m = 10\ \mathrm{cm^2\ g^{-1}}$ (discussed in Section 3) are depicted at $z = 0$.

species (Section 2). The difference in density, and therefore DM scattering rate, can vary by up to 60 per cent from the spherically averaged value, depending on the flattening (Appendix A).

To compute the density ρ, we use the mass enclosed in shells that follow the triaxial ellipsoidal surfaces calculated using the method described in Section 2, which approximately follow isodensity surfaces. However, we use much broader spacing in distance for the density calculation than for the ellipsoid fits, spacing shells by roughly every 10th point in r for which a fit is carried out, to allow enough space between shells to get sufficient numbers of particles and to mitigate problems caused by the twisting of the ellipsoid axes between shells. To estimate the density at ellipsoidal distance d_κ, we select all particles N_κ within a shell κ centred on the ellipsoid with semimajor axis a_κ (discarding shells with $N_\kappa < 100$). The shell half-thickness $\Delta\mathrm{d}_\kappa$ is set by the difference in semimajor axis between the isodensity surface at d_κ and its inner neighbour, such that $\Delta\mathrm{d}_\kappa \equiv a_\kappa - a_{\kappa-1}$. Then the density $\rho(\mathrm{d}_\kappa)$ is computed as

$$\rho(\mathrm{d}_\kappa) \equiv \frac{\sum_{n=1}^{N_\kappa} m_n}{\frac{4}{3}\pi q_\kappa s_\kappa \left[(\mathrm{d}_\kappa + \Delta\mathrm{d}_\kappa)^3 - (\mathrm{d}_\kappa - \Delta\mathrm{d}_\kappa)^3\right]}, \quad (4)$$

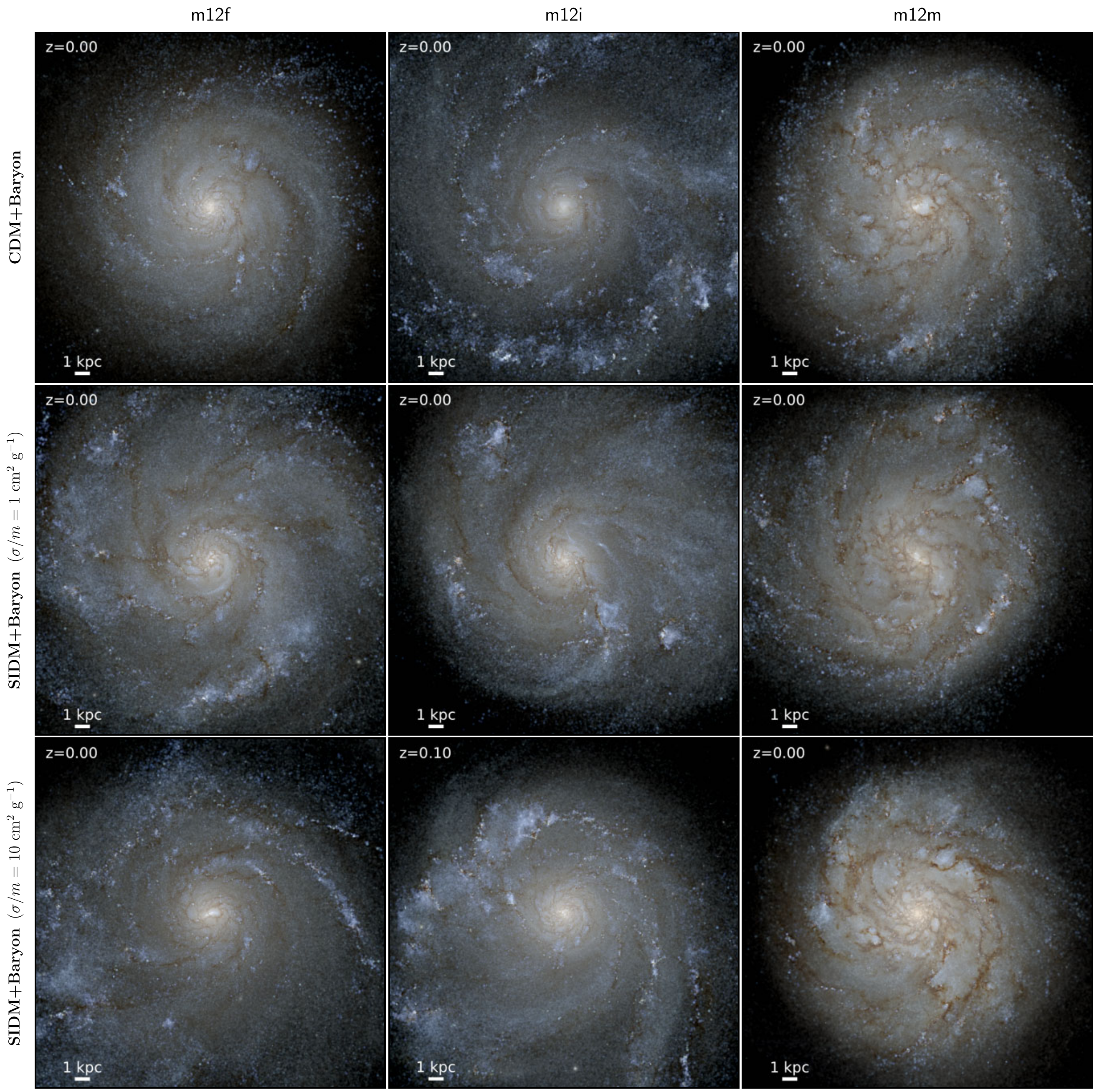

Figure 2. Face-on disc view of cosmological-baryonic simulated MW-mass galaxies. SED-modeled, ray-traced images of starlight in three sets of MW-mass galaxy simulations: `m12f` (left), `m12i` (centre), and `m12m` (right); all DM+Baryon simulations are shown except `m12m` SIDM+Baryon $\sigma/m = 0.1$ cm^2 g^{-1} (which is quite similar to the `m12m` CDM+Baryon case). Each panel is 30 kpc across and the galaxy has been rotated to show the disc face-on. All simulations except `m12i` SIDM+Baryon $\sigma/m = 10$ cm^2 g^{-1} (discussed in Section 3) are depicted at $z = 0$.

where q_κ and s_κ are the axis ratios of the ellipsoid used to calculate d_κ. Likewise the RMS velocity $v_{\mathrm{rms}}(\mathrm{d}_\kappa)$ is

$$v_{\mathrm{rms}}(\mathrm{d}_\kappa) \equiv \sqrt{\frac{1}{N_\kappa}\sum_{n=1}^{N_\kappa} \mathbf{v}_n \cdot \mathbf{v}_n}\,, \tag{5}$$

where $\mathbf{v}_n$ is the velocity vector of particle n inside shell κ.

We also calculate the DM local collision rate,

$$\begin{aligned}\Gamma_{\mathrm{scatter}}(d) &= \rho_{\mathrm{DM}}(d)\, v_{\mathrm{rel}}(d)\, \sigma/m \\ &\approx \frac{4}{\sqrt{3\pi}}\, \rho_{\mathrm{DM}}(d)\, v_{\mathrm{rms}}(d)\, \sigma/m\,,\end{aligned} \tag{6}$$

where $\rho_{\mathrm{DM}}(d)$ is the DM density and $v_{\mathrm{rel}}(d)$ is the relative DM velocity. We approximate v_{rel} by $4/\sqrt{3\pi}\, v_{\mathrm{rms}} \approx 1.3\, v_{\mathrm{rms}}$, which holds exactly for a Maxwellian velocity distribution. We define the LCR scattering radius d_1 by requiring $\Gamma_{\mathrm{scatter}}(d_1) = t_{z=0}^{-1}$, where t_z is the time at redshift z, thus $t_{z=0} = 13.8$ Gyr is age of the Universe

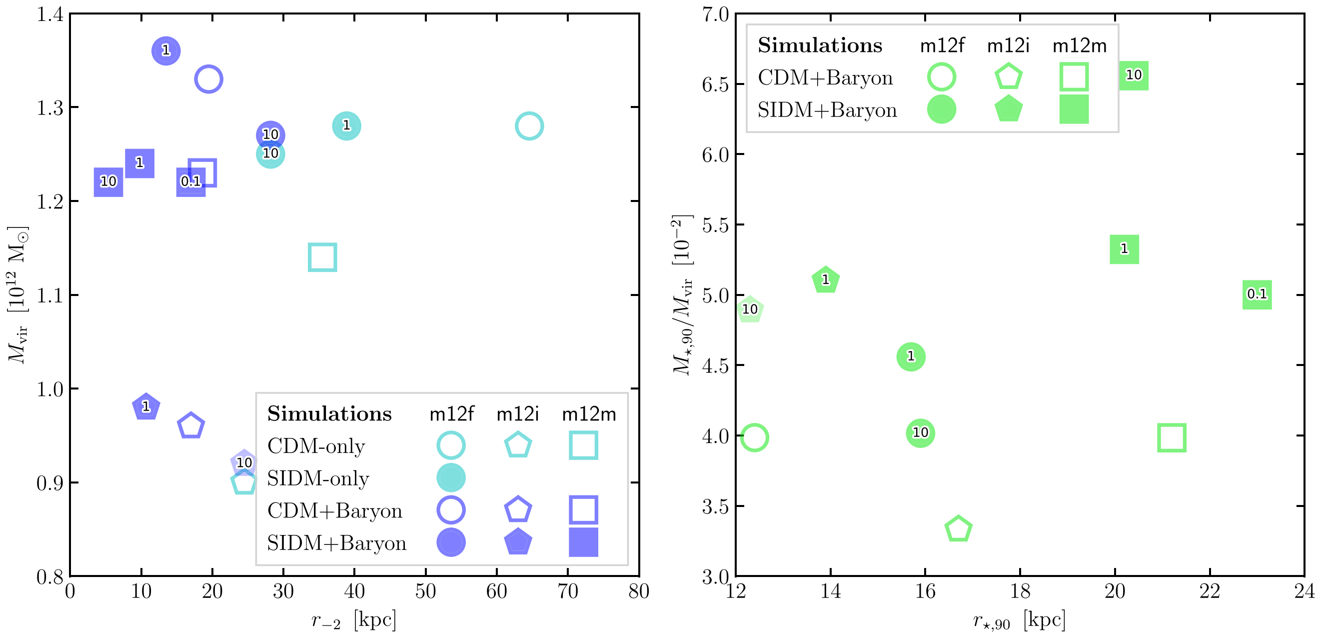

Figure 3. Global DM and stellar properties of simulated MW-mass galaxies. DM virial mass $M_{\rm vir}$ as a function of DM scale radius r_{-2} (left) and stellar-to-halo mass ratio $M_{\star,\,90}/M_{\rm vir}$ as a function of radius enclosing 90 per cent of stellar mass (right) for `m12f` (circles), `m12i` (pentagons), and `m12m` (squares). In the left-hand panel (DM properties), the CDM-only, SIDM-only, CDM+Baryon, and SIDM+Baryon simulations are represented with hollow cyan, solid cyan, hollow blue, and solid blue markers, respectively; in the right-hand panel (stellar properties), the CDM+Baryon and SIDM+Baryon simulations are represented with hollow green and solid green markers, respectively. In both panels, the SIDM+Baryon simulations with $\sigma/m = 0.1$, 1, and 10 cm^2 g^{-1} are shown with these respective numbers inside the markers. The simulation of `m12i` SIDM+Baryon at $\sigma/m = 10$ cm^2 g^{-1} is evaluated at $z = 0.1$ (instead of $z = 0$ like all other simulations), indicated with a decrease in alpha (lighter shade).

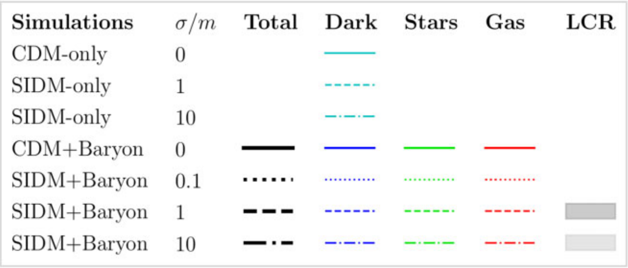

Simulations	σ/m	Total	Dark	Stars	Gas	LCR
CDM-only	0		—			
SIDM-only	1		- - -			
SIDM-only	10		-·-			
CDM+Baryon	0	—	—	—	—	
SIDM+Baryon	0.1	·····	·····	·····	·····	
SIDM+Baryon	1	- - -	- - -	- - -	- - -	▨
SIDM+Baryon	10	-·-	-·-	-·-	-·-	░

Figure 4. Legend for comparisons of simulated MW-mass galaxies in CDM and SIDM. Line-styles denote different DM cross-sections listed above in units of cm^2 g^{-1}, colours show the different species, and shaded areas indicate the SIDM LCR. These line-styles, colours, and shaded areas are used throughout the rest of this work and the Appendix.

(Planck Collaboration 2014, table A.1: *Planck*+WP+BAO).[3] Thus, inside d_1, DM particles have experienced at least one self-scatter within the age of the Universe (based on the density distribution at $z = 0$), giving an approximate volume inside which we expect the SIDM differences to be the largest. The d_1 for different simulations are given in Table 1, and the LCR for different SIDM+Baryon σ/m are represented as grey shaded areas (as shown by the legend in Fig. 4) and used in all subsequent and relevant Figs in this work and the Appendix.

As expected, the SIDM-only density profiles for `m12f` (Fig. 5, left) have much lower densities in the central region compared to all the other DM profiles, while the DM profiles in all the CDM-only, CDM+Baryon, and SIDM+Baryon simulations are remarkably similar. The CDM-only and SIDM-only densities are too low to produce smooth curves for $r \lesssim 2$ kpc.

In the simulations with baryons, the density of stars dominates the central region, while the DM and gas approximately follow each other about a magnitude below the stellar component. The stellar mass density of `m12m` is lower in the central region and higher at larger radii compared to that of `m12f` and `m12i`. Notably, when examining the bottom row showing ρd^2, there does not appear to be a transition at d_1 from an isothermal (flat in this view) profile at $r < d_1$ to a Navarro–Frenk–White (NFW)-like profile at $r > d_1$, as posited in Spergel & Steinhardt (2000). This is another illustration of the effect of the growing galaxy in the centre in altering the density profile well beyond the baryon-dominated region, thanks to the significant radial anisotropy in the DM velocity distribution.

RMS velocity profiles are shown in Fig. 6. The CDM-only and SIDM-only simulations have much lower central RMS velocities than the corresponding DM curves in the CDM+Baryon and SIDM+Baryon simulations, except in the extreme outskirts ($r \gtrsim 100$ kpc). The additional component added by the baryons deepens the central potential and subsequently increases the DM density, leading to higher RMS velocities. The biggest differences are between CDM-only and CDM+Baryon in the central region for `m12f` and `m12i`. The velocity dispersion in the CDM+Baryon case is much higher than for CDM-only in both these simulations due to baryonic deepening of the potential. In the SIDM case, the effects of baryonic contraction are offset by the ability of the DM to thermalize;

---

[3] `m12i` SIDM+Baryon $\sigma/m = 10$ cm^2 g^{-1} is evaluated at $z = 0.1$, which gives $\Gamma_{\rm scatter}(d_1) = t^{-1}_{z=0.1}$ where $t_{z\,=\,0.1} = 12.5$ Gyr.

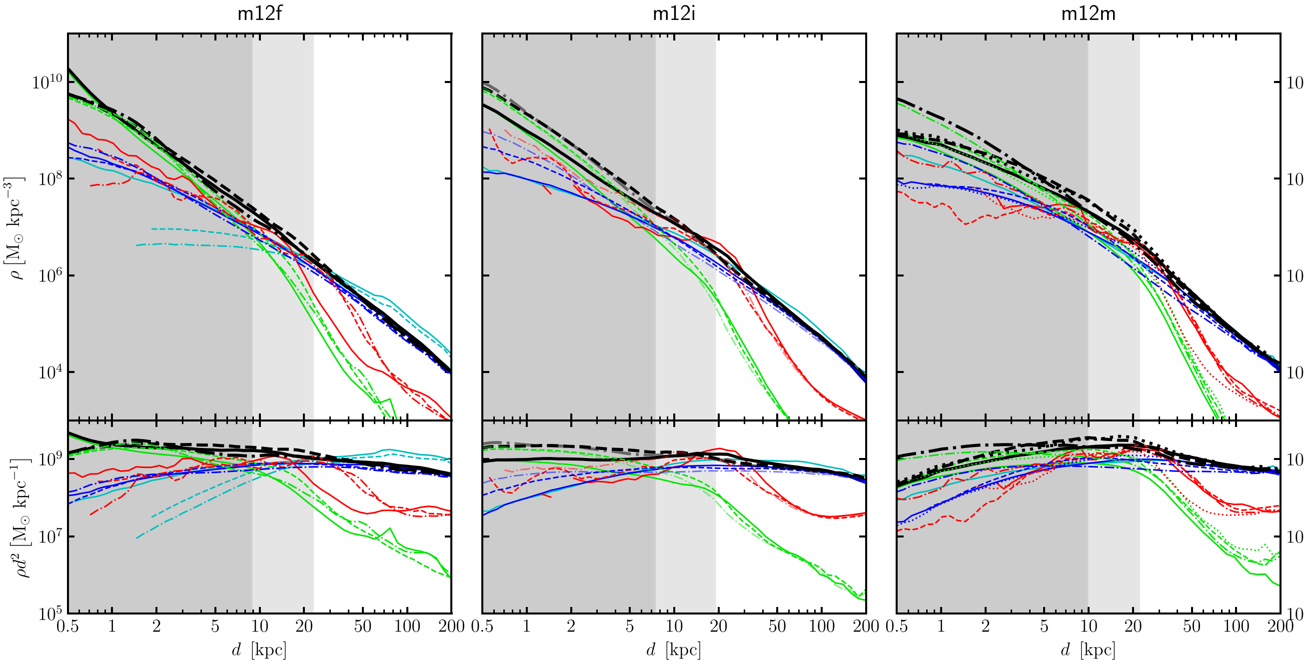

Figure 5. Ellipsoidally averaged density profiles of the simulated MW-mass galaxies. Density ρ (top) and ρd^2 (bottom; an ideal isothermal profile is flat in this view) as a function of ellipsoidal distance d for `m12f` (left), `m12i` (centre), and `m12m` (right). Line-styles, colours, and shaded areas follow the legend in Fig. 4.

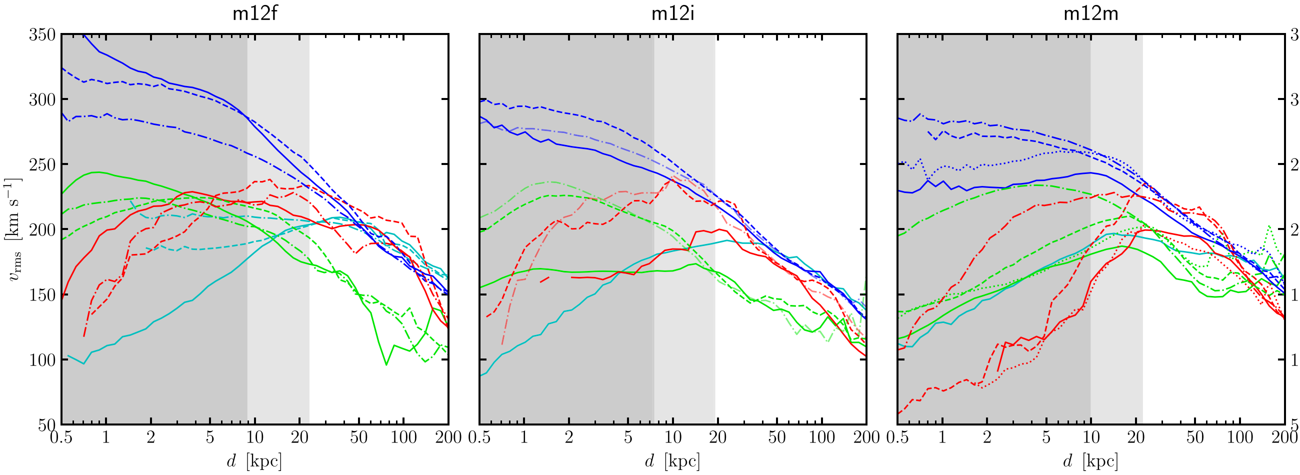

Figure 6. Ellipsoidally averaged velocity profiles of the simulated MW-mass galaxies. Root-mean-square (RMS) velocity $v_{\rm rms}$ as a function of ellipsoidal distance d for `m12f` (left), `m12i` (centre), and `m12m` (right). Line-styles, colours, and shaded areas follow the legend in Fig. 4.

that is, to transfer some of the energy outward that would otherwise go into raising the central velocity dispersion. Surprisingly, for `m12m`, the SIDM+Baryon runs have significantly larger central velocity dispersion than the CDM+Baryon run does. This is probably related to the fact that the central galaxy in `m12m` is substantially more massive as σ/m increases without becoming significantly larger in extent (Fig. 3), implying that the average stellar density is larger in the SIDM+Baryon runs than the CDM+Baryon one. Indeed, the central galaxy in `m12i` shows the same tendency for the SIDM systems to be slightly more massive in stellar mass, but has slightly less variation between DM models than `m12m`. This variety illustrates how the central density and velocity dispersion of the DM are shaped by interplay with the growing galaxy in the centre of the halo.

Fig. 7 shows the local collision rate $\Gamma_{\rm scatter}$ as a function of ellipsoidal distance d. The scattering radius d_1 is smaller for $\sigma/m = 1$ cm^2 g^{-1} than 10 cm^2 g^{-1}, while the rate for 0.1 cm^2 g^{-1} is less than $t^{-1}_{z=0}$ at all radii for the $z = 0$ density distribution (though this is not necessarily true at all z). The profile for `m12f` SIDM-only $\sigma/m = 1$ cm^2 g^{-1} also does not reach $t^{-1}_{z=0}$, while 10 cm^2 g^{-1} does. This indicates that while self-interactions may have occurred earlier, the resulting heating reduces the scattering rate by $z = 0$ to less than $t^{-1}_{z=0}$ everywhere. On the other hand, all SIDM haloes with baryons have substantially higher interaction rates at the present day, likely as a result of the additional depth in the gravitational potential created by the central galaxy. The growing galaxy can thus amplify the effect of a nonzero SIDM cross-section in the

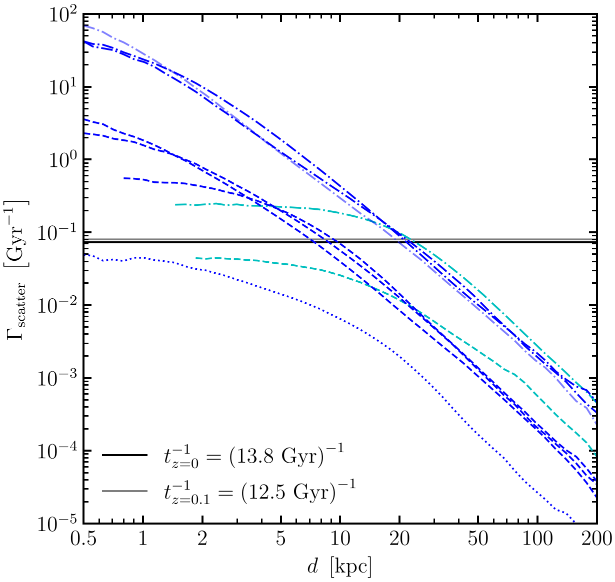

Figure 7. Ellipsoidally averaged DM local collision rate profiles of the simulated MW-mass SIDM galaxies. The local DM self-scattering rate $\Gamma_{\rm scatter}$ (equation 6) is shown as a function of ellipsoidal distance d for SIDM simulations. Line-styles and colours follow the legend in Fig. 4. The point where $\Gamma_{\rm scatter}$ intersects the grey horizontal lines at $t_{z=0}^{-1}$ and $t_{z=0.1}^{-1}$ marks the scattering radius d_1, shown as the shaded areas of all subsequent and relevant Figs in this work and the Appendix.

central portion of the halo by keeping the scattering rate higher over time.

4.2 Shape profiles

The profiles for the minor-to-major axial ratio, $s = c/a$, for the different haloes in the simulations are shown in Fig. 8. As summarized in Fig. 4, different colours distinguish between simulations with and without baryons and among species (DM, stars, and gas), while line-styles show different DM interaction cross-sections σ/m. Axis ratios are calculated using the method described in Section 2, and we remove all data points where the triaxial ellipsoids do not enclose at least 5000 particles (see appendix A of Vera-Ciro et al. 2011, where at least 3000 particles are used).

Axis ratio differences between the CDM+Baryon and SIDM+Baryon simulations are small compared to the differences between the CDM-only and SIDM-only simulations over the same range of cross-sections (Fig. 8). SIDM-only creates the most spherical DM haloes, obtained for the highest σ/m. Adding baryons to these simulations increases the overall roundness, but increasing σ/m does not produce the large changes seen in the non-baryon cases. The effect of the growth of the central galaxy is to standardize the shape in roughly the same range of axis ratios, between approximately 0.6 and 0.8. In `m12f` (left) and `m12i` (centre), most of the scaling of the shape with cross-section is also erased. In `m12m` (right) there are still substantial differences between haloes with different cross-sections, but the variation in shape has been 'recentred' around the CDM case, while with DM-only the shape just gets progressively rounder for larger cross-sections.

In the central region of these MW-mass galaxies ($r \lesssim 10$ kpc), CDM+Baryon produces a more spherical DM distribution than SIDM+Baryon in nearly all cases. This is consistent with, though less pronounced than, the effects discussed in Sameie et al. (2018), but contrary to expectations from analytic predictions considering only DM (Tulin & Yu 2018). The *stellar* distribution is also frequently flatter for SIDM than CDM across all three galaxies. These differences are greatest in the region where SIDM is collisional (grey shaded areas), and the degree of flattening in the DM distribution parallels the flattening in the stars, indicating ongoing dynamical coupling between the stellar and DM distributions in the inner galaxy.

It is also apparent from the shape curves, which stop when the ellipsoid no longer encloses at least 5000 particles, that the SIDM haloes with baryons remain much denser in their centres at late times than those without baryons (as discussed in Section 4.1). The LCR grey shaded areas are calculated from the *present-day* DM densities (Fig. 6), indicating that while the SIDM-only haloes have reached an equilibrium where even their innermost regions have a very low collision rate relative to the age of the Universe, the gradually increasing potential depth due to the central galaxy counteracts collisional heating and maintains a much higher central collision rate at late times. This also supports the idea that there

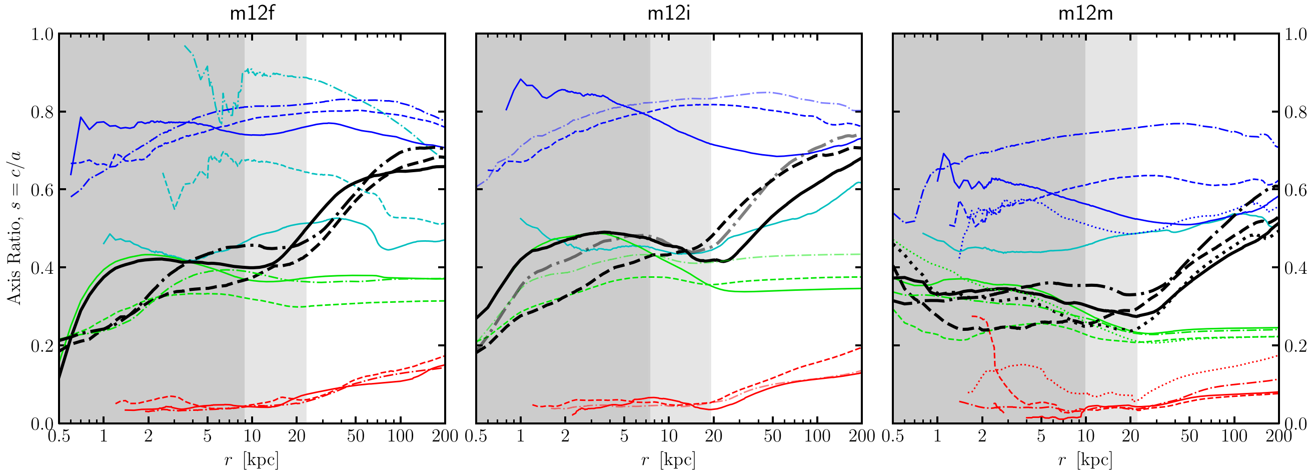

Figure 8. Shape profiles of simulated MW-mass galaxies. Minor-to-major axial ratio $s = c/a$ is shown as a function of semimajor axis $r = a$ for different species (DM, stars, and gas) in three sets of MW-mass galaxy simulations: `m12f` (left), `m12i` (centre), and `m12m` (right). Line-styles, colours, and shaded areas follow the legend in Fig. 4. An alternate version of this plot using the geometrical mean of the axis lengths, $R = (abc)^{1/3}$, can be found in Appendix B.

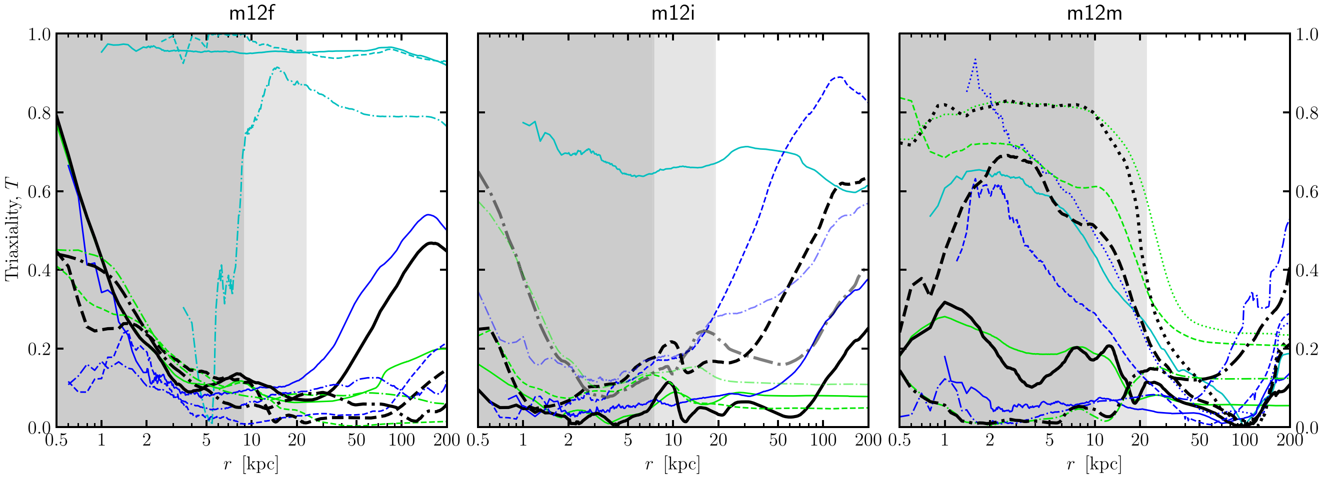

Figure 9. Triaxiality profiles of simulated MW-mass galaxies. Triaxiality T is shown as a function of semimajor axis $r = a$ for different species (DM and stars) in three sets of MW-mass galaxy simulations: `m12f` (left), `m12i` (centre), and `m12m` (right). Line-styles, colours, and shaded areas follow the legend in Fig. 4. An alternate version of this plot using the geometrical mean of the axis lengths, $R = (abc)^{1/3}$, can be found in Appendix B.

is ongoing information exchange between the DM and stars in the inner galaxy, and suggests that this region may not be in equilibrium between the two species.

The `m12m` series of simulations contains most of the exceptions to these generalizations and is thus worth discussing in more detail. This galaxy is the earliest of the three to form and has the largest scale radius (Fig. 3), meaning that its baryonic component has had the longest time to shape the DM distribution (and vice versa) over the largest range of radii. As pointed out in Section 3, its global properties have the opposite trend with σ/m from the other two haloes. It is also the only halo whose outer shape ($\gtrsim 20$ kpc) is consistent between the CDM-only and CDM+Baryon cases, and the only one where there is significant variation of the shape with cross-section across all radii. Its particular assembly history (early accretion of many small galaxies) thus appears particularly sensitive to SIDM effects. This could be because it simply has more time to establish equilibrium between the SIDM and stellar components, and is driven there more rapidly by a central relatively large galaxy that forms early.

A full comparison of the central DM shapes in these simulations is challenging, since many of the profiles are noisy due to low particle number. This is especially true for the `m12f` SIDM-only simulations, whose shape profiles inside 5–10 kpc are ambiguous thanks to their low central densities. In all the DM+Baryon simulations, the shape of the stellar component is well resolved (at all radii) and closely follows the shape of the *total* mass distribution (at lower radii), which is accessible through dynamical modeling. We will examine in more detail whether the differences in the 3D shape of the *stellar* distribution are observable in future work.

4.3 Triaxiality

To better understand the shapes, we also calculate the triaxiality parameter T (Franx, Illingworth & de Zeeuw 1991),

$$T \equiv \frac{a^2 - b^2}{a^2 - c^2} = \frac{1 - q^2}{1 - s^2}\,, \tag{7}$$

where an ellipsoid is oblate if $0 < T < 1/3$ ($T = 0$ is a perfect oblate distribution, $c \ll a = b$), triaxial if $1/3 < T < 2/3$ ($T = 0.5$ is a maximally triaxial distribution), and prolate if $2/3 < T < 1$ ($T = 1$ is a perfect prolate distribution, $b = c \ll a$). Fig. 9 shows the triaxiality for the stellar and DM components of all simulations, as well as the total mass distribution. There are a wide variety of behaviors on display. Consistent with our other results, `m12m` has significantly different behaviour than `m12f` and `m12i`.

The DM-only haloes for all three set of simulations are highly prolate or triaxial in the centre, especially `m12f`. For CDM, this triaxiality/prolateness is well understood. Interestingly, though, at large radii `m12i` and `m12f` stay relatively triaxial while the `m12m` CDM-only halo transitions to an oblate shape, which is unusual for a typical CDM-only simulated halo at this mass scale. The DM+Baryon haloes `m12f` and `m12i` tend to be quite oblate at intermediate radii ($2 \lesssim r \lesssim 50$ kpc), with very little difference between DM models. At large radii ($r \gtrsim 50$ kpc) most haloes (even `m12m`) transition to a somewhat more triaxial shape. This is also expected since the SIDM interaction rates (Fig. 7) are quite low at these distances, so the DM behaviour should not differ appreciably from CDM. The degree of triaxiality at large radii varies substantially, however, with no clear trend with σ/m.

In the inner regions of the haloes, `m12f` shows significant triaxiality in the CDM+Baryon case and more oblate structure in the SIDM+Baryon cases, while in `m12m` there is a huge variation in the degree of triaxiality in the central part of the halo. Interestingly, the triaxiality of the *total* mass distribution does not universally follow the stellar distribution in the inner galaxy the way that the $s = c/a$ axial ratio does.

4.4 Comparison to previous work

We first compare the DM shape profiles to previous results from DM-only simulations, those with an analytic disc model, and CDM+Baryon simulations (see Sameie et al. 2018, fig. 7 for a summary). In Fig. 10, we plot the shape of the DM component for all the FIRE-2 MW-mass galaxy simulations of Table 1. This comparison uses log-scale for the y-axis axial ratio $s = c/a$ and geometric mean of the axis lengths $R = (abc)^{1/3}$ for the x-axis, for direct comparison with the summary in fig. 7 of Sameie et al. (2018). Plots of the axial ratio $s = c/a$ and triaxiality T versus geometric mean radius R for all individual species are given in Appendix B.

We see a clear trend towards more spherical haloes at larger σ/m for the DM-only simulations, but find that the SIDM+Baryon

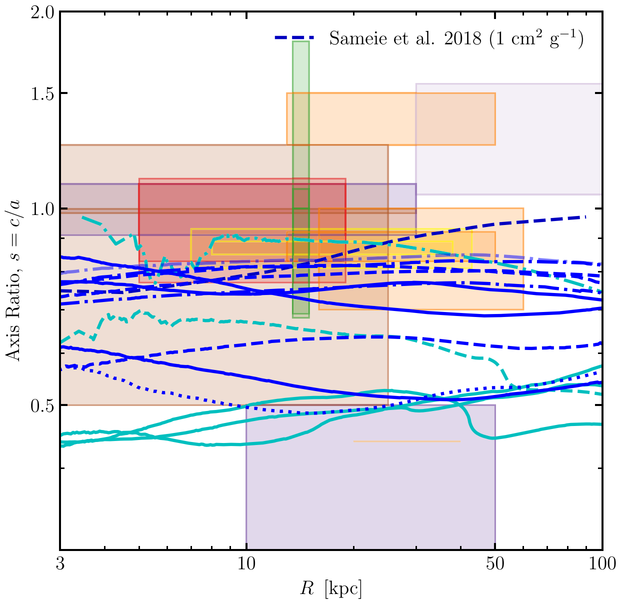

Figure 10. Shape profiles of DM in simulated MW-mass galaxies compared to estimates for the MW. Axis ratio $s = c/a$ is shown as a function of geometrical mean radius $R = (abc)^{1/3}$ for the DM component in all simulations. Line-styles and colours follow the legend in Fig. 4 (but with thicker lines) for the simulations. The dark blue dashed-line follows a previous SIDM+Baryon semi-analytic model for $\sigma/m = 1$ cm^2 g^{-1} (see fig. 7 of Sameie et al. 2018). The SIDM+Baryon simulations are generally more spherical than CDM-only, but not notably different than CDM+Baryon, and show less variation with σ/m than in SIDM-only. All simulations except CDM-only are loosely consistent with the various estimates for the MW. For simulations with baryons, halo-to-halo variation is comparable to the difference between DM models. The estimated values of the halo density flattening parameter $q_\rho^{\rm DM} = (c/a)_\rho$ are summarized in Table 2, and are plotted over their approximate regions of validity (i.e. the range spanned by the data used for the constraints). The coloured boxes and lines indicate the various estimates for $q_\rho^{\rm DM} = (c/a)_\rho$ summarized in Table 2. Constraints derived from models of individual tidal streams are shown in orange (Sagittarius stream), red (Palomar 5 stream), green (Grillmair-Dionatos-1 stream), and yellow (statistically detected streams around NGC 3201 and M68). Constraints based on Jeans modeling are shown in purple, and measurements combining equilibrium assumptions with the disc rotation curve and/or other disc data are shown in brown.

simulations are not as spherical at larger radii as assumed in the SIDM+Baryon semi-analytic model of Sameie et al. (2018), which is initialized with a spherically symmetric halo. Also, instead of the concave-up shape predicted by this model for SIDM+Baryon (with the innermost and outermost regions the most spherical), we see a concave-down trend for all the curves (where the intermediate radii are most spherical). This appears consistent with the idea that SIDM can respond more quickly to the influence of the central galaxy than CDM (which generally has a more spherical inner halo when compared across resimulations of the same initial conditions). It is also consistent with the picture that CDM and SIDM should behave similarly in the halo outskirts, where the shape is driven mainly by the connection with the local filaments (see e.g. Vera-Ciro et al. 2011) and therefore tends to be less spherical than at intermediate radii. However, the variation in formation histories across the different haloes dominates over the variation with σ/m.

We also compare our results to estimates of the halo density flattening parameter (minor-to-major axial ratio) $q_\rho^{\rm DM} = (c/a)_\rho$ from the literature, summarized in Table 2. This quantity is sometimes referred to in the literature (see e.g. Hattori, Valluri & Vasiliev 2021) as simply parameter q, but is changed here to distinguish from our intermediate-to-major axial ratio $q(r) = b(r)/a(r)$. In modeling the kinematics of various MW tracers of the potential such as tidal streams, globular clusters, or ‘field’ halo stars unassigned to a given stream, the parameter $q_\rho^{\rm DM}$ usually represents the flattening of the best-fitting axisymmetric NFW model for the DM density, and is comparable to our minor-to-major axial ratio $s(r) = c(r)/a(r)$. In the case of Law & Majewski (2010), where a triaxial halo is used, we cite the value of $(c/a)_\rho$ quoted by the authors within 20 kpc, which was determined by fitting ellipsoids to the contours of the Laplacian of the potential.

The various estimates for the shape of the MW (given by the references of Table 2) vary as widely as shapes of the simulated galaxies, underlining the difficulty of the measurement. These measurements have a wide spread in both r and $q_\rho^{\rm DM}$, and thus, don’t agree on the shape (or the triaxiality) of the MW. One positive development from this work is that in most DM models the value of $s = c/a$ for the DM haloes of the simulated systems appears to be fairly constant ($\Delta s \lesssim 0.2$) over a wide range of radii (3–100 kpc), which should in principle simplify efforts to model the dark halo. We caution, however, that (1) none of our models include a Large Magellanic Cloud (LMC)-like companion, which is likely to affect this assertion (e.g. Law & Majewski 2010; Vera-Ciro & Helmi 2013; Vasiliev, Belokurov & Erkal 2021) and (2) that this statement assumes that any rotation of the principal axes with radius is precisely incorporated into the model.

5 DISCUSSION

The presence of baryons, and their resulting effect on the shapes of MW-mass galaxies, shows far wider variety than expected from DM-only and semi-analytic models. Importantly, MW-mass galaxies in SIDM haloes at the preferred values of σ/m based on studies of dwarf galaxies and galaxy clusters still have density, velocity, and shape profiles that are consistent with observations, as well as producing a realistic-looking disc galaxy at the centre. Thus, there is no immediate discrepancy produced by the introduction of a nonzero self-interaction cross-section (at least in the velocity-independent, elastic collision model considered here) that can rule out this type of SIDM.

More interesting is the question of whether the variation in shape due to a nonzero cross-section could be constrained well enough to differentiate SIDM from CDM. From Fig. 10 the hope of doing this seems fairly dim, since there is as much variation in shape from different assembly histories as from different DM models. However, the importance of the question merits a closer look at comparisons involving the particular radii where we expect the differences to be largest.

The key region for looking at shape variations produced by SIDM is likely to be between about 2–20 kpc, still inside d_1 (so the self-interactions have a chance to shape the system), but outside the region where the shape is utterly dominated by the central galaxy’s baryons. We have the advantage that in this region we can still tightly constrain the shape of the stellar and gas components from observations, and look instead at where the shape of the total mass distribution (constrained using dynamical modeling) departs from the shape of the stars.

Table 2. Measurements of the shape of the MW halo from previous work. Uncertainties on $q_\rho^{\rm DM} = (c/a)_\rho$ parameter values are quoted as given in the various works and plotted in Fig. 10, which usually correspond to 90 per cent confidence intervals or equivalent. Values with no uncertainties have no easily interpretable range given in the corresponding paper, or are lower limits. $r_{\rm min}$ and $r_{\rm max}$ denote the approximate range of Galactocentric radii over which the estimates are made, either as given by the authors or as specified for the data set used.

Reference	$q_\rho^{\rm DM} = (c/a)_\rho$	$r_{\rm min}$ [kpc]	$r_{\rm max}$ [kpc]	Data set used	Colour
Hattori et al. (2021)	$0.993^{+0.01}_{-0.005}$	1	30	RR Lyrae + constraints[a]	Brown
Palau & Miralda-Escudé (2021)	$0.87^{+0.02}_{-0.02}$	8	38	NGC 3201[b]	Yellow
Malhan & Ibata (2019)	$0.82^{+0.25}_{-0.13}$	13.5	15	Grillmair-Dionatos-1 (GD-1)	Green
Posti & Helmi (2019)	$1.30^{+0.25}_{-0.25}$	30	150	Globular clusters[c]	Purple
Wegg, Gerhard & Bieth (2019)	$1.00^{+0.09}_{-0.09}$	1	30	RR Lyrae	Purple
Palau & Miralda-Escudé (2019)	$0.87^{+0.06}_{-0.06}$	7	43	M68[b]	Yellow
Bovy et al. (2016)	$1.3^{+0.5}_{-0.3}$	13.5	15	Grillmair-Dionatos-1 (GD-1)	Green
Bovy et al. (2016)	$0.93^{+0.16}_{-0.16}$	5	19	Palomar 5 (Pal 5)	Red
Küpper et al. (2015)	$0.95^{+0.16}_{-0.12}$	5	19	Palomar 5 (Pal 5)	Red
Loebman et al. (2014)	$0.4^{+0.1}_{-0.1}$	10	50	SDSS halo stars	Purple
Koposov, Rix & Hogg (2010)	>0.68	13.5	15	Grillmair-Dionatos-1 (GD-1)	Green
Law & Majewski (2010)	0.44	20	40	Sagittarius (Sgr)[d]	Orange
Johnston, Law & Majewski (2005)	$0.88^{+0.04}_{-0.05}$	13	50	Sagittarius (Sgr)	Orange
Helmi (2004)	$1.30^{+0.20}_{-0.05}$	13	50	Sagittarius (Sgr)	Orange
Ibata et al. (2001)	>0.7	16	60	Sagittarius (Sgr)	Orange
Olling & Merrifield (2000)	$0.80^{+0.45}_{-0.30}$	1	25	H I gas + disc rotation curve	Brown

[a] This paper includes the rotation curve, velocity dispersion, and vertical force profile of the disc as additional constraints. [b] In these two cases, a flattening of $q_\rho^{\rm DM} = 0.8$ in the density was assumed to detect the stream statistically before using it to fit a parametrized mass model. [c] As pointed out by Hattori et al. (2021), this paper finds a prolate aspect ratio using an action finder that has known difficulties for orbits in prolate mass distributions. [d] As Law & Majewski (2010) point out and Debattista et al. (2013) confirm, this model does not admit a stable Galactic disc; Vera-Ciro & Helmi (2013) shows that the discrepancy can be explained by the influence of the LMC.

We do this by plotting the difference between the total and stellar axis ratios $\Delta s = s_{\rm tot} - s_\star$ in Fig. 11. The region $r < 5$ kpc is dominated by the bulge dynamics and hence varies substantially between galaxies. However, outside this region we see that there are clear transitions in the slope for all the curves between the flattened, stellar-disc-dominated regime (out to around 20 kpc) and the region where the total shape is determined by the more spherical DM halo. For CDM+Baryon simulations, the transitions roughly occur at $r_{\star,90}$, represented by the green vertical lines. For the SIDM+Baryon simulations, the transitions roughly occur at d_1, represented by the shaded areas, following the legend in Fig. 4. While the CDM+Baryon transitions are largely dependent on the stellar mass, the SIDM+Baryon transitions are instead dependent on the DM self-interaction cross-section. This holds for $\sigma/m = 1$ and $10\,{\rm cm^2\,g^{-1}}$, but not for the `m12m` SIDM+Baryon $\sigma/m = 0.1\,{\rm cm^2\,g^{-1}}$, which has no detectable d_1 at $z = 0$. Since the density for $\sigma/m = 0.1\ {\rm cm^2\,g^{-1}}$ does not reach the levels needed for local collisions to occur within the age of the halo, this cross-section behaves similarly to CDM and the shape transition occurs at $r_{\star,90}$. Likewise, constructing such a test would be difficult near $\sigma/m = 10\,{\rm cm^2\,g^{-1}}$ in `m12m` since d_1 and $r_{\star,90}$ are very close in this case. Otherwise, we see that for SIDM+Baryon, across all three simulations, *the shape of the total mass distribution departs from that of the stellar mass distribution at steadily increasing radius as σ/m increases*. Thus, for a given galaxy, constraining the radius of the transition from where stars dominate its shape to where DM is the dominant influence and comparing this to (1) the galaxy scale length and (2) the predicted d_1 as a function of σ/m provides a way to constrain the SIDM cross-section.

Currently, there are several methods in use for constraining the shape of the MW's total mass distribution using dynamical modeling. A non-exhaustive sample of measurements using these different methods is listed in Table 2. One strategy is to model the precession of the orbital planes of tidal streams. Several attempts to do this for the Sagittarius stream alone (Helmi 2004; Johnston et al. 2005; Law, Majewski & Johnston 2009; Vera-Ciro & Helmi 2013; Vasiliev et al. 2021) have come to inconsistent conclusions, mostly due to differing parametrizations of the potential and the treatment of the influence of the LMC on the outer portion of the stream (as pointed out in Vera-Ciro & Helmi 2013 and Erkal, Belokurov & Parkin 2020). However, since we need mainly to constrain the region $2 \lesssim r \lesssim 20$ kpc for these tests, simultaneous fits of several streams with smaller apocentres may provide a way forward (Bovy et al. 2016; Bonaca & Hogg 2018; Reino et al. 2021).

Another strategy is to constrain the total flattening using Jeans or Schwarzschild modeling of equilibrium stellar populations as in Loebman et al. (2014), Hattori et al. (2021), and many other works. However, this is limited to regions where we have sufficient stellar tracers observed to derive the distribution functions used in the model. Currently such efforts have been made in the bulge (to $r \sim 5$ kpc) and in the space observatory Gaia satellite's 6D volume ($5 \lesssim r \lesssim 11$ kpc). However, additional data from ground-based spectroscopic surveys, future Gaia data releases, and new distance estimators (e.g Das & Sanders 2019; Auge et al. 2020) promise to expand the volume accessible to this technique appreciably in the near future. These new data will also provide excellent constraints on the *stellar* shape profile, an equally important quantity in this approach.

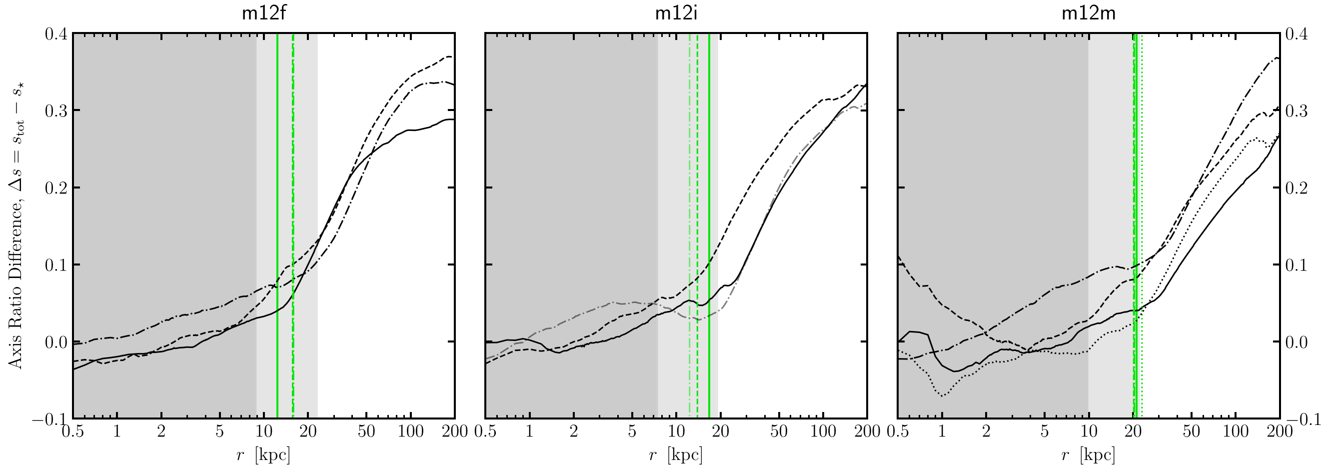

Figure 11. Difference in shape profiles of simulated MW-mass galaxies. Minor-to-major axial ratio difference $\Delta s = s_{\rm tot} - s_\star$ is shown as a function of semimajor axis $r = a$ in three sets of MW-mass galaxy simulations: `m12f` (left), `m12i` (centre), and `m12m` (right). Line-styles and shaded areas follow the legend in Fig. 4. The black curves represent the axial ratio difference Δs and the vertical lines represent $r_{\star,\,90}$, the spherical radius of 90 per cent of stellar mass within 30 kpc of the central galaxy, given in Table 1.

A third strategy, as employed by e.g. Blitz & Spergel (1991), Olling & Merrifield (2000), Narayan, Saha & Jog (2005) in the MW and Das et al. (2020) for external galaxies, is to use the flaring of the H I disc to constrain the flattening, under the assumption that the gas is in dynamical equilibrium. Results seem to favour a relatively spherical halo with $q_\rho^{\rm DM} \sim 0.8$. This technique could provide an independent assessment with different data and systematics than methods using stellar kinematics.

Finally, a lower limit on $s = c/a$ as a function of radius may be obtained by searching for evidence of the truncation or scattering of tidal streams by orbital resonances, which are more common in more highly flattened potentials (Valluri et al. 2012; Pearson et al. 2015; Hesp & Helmi 2018; Valluri, Price-Whelan & Snyder 2021). These effects are quite pronounced at $c/a \sim 0.3$–0.4, where most of our shape profiles begin their transition toward the more spherical halo, and are much less dominant by $c/a \sim 0.6$–0.7, where most of the total mass profiles end up at large r. Looking for an abrupt transition in the prevalence of streams as a function of Galactocentric distance, perhaps even in a stacked sample of external galaxies where 6D information is not available, could be an additional way to find constraints on the halo flattening transition and hence on SIDM.

6 CONCLUSION

We perform a suite of cosmological-baryonic zoom simulations of MW-mass galaxies for several different models with SIDM, one proposed solution to the challenges of the CDM plus dark energy (ΛCDM) cosmological model at small-scales. These DM simulations are compared between CDM and SIDM (with interaction cross-sections $\sigma/m = 0.1$, 1, and 10 cm^2 g^{-1}) and with expectations from the literature.

For the SIDM+Baryon simulations, the variation in axial ratio with SIDM cross-section is not as large as expected in the literature. The assembly history of the central galaxy is the dominant influence inside the LCR. Variations in the assembly and evolution of the galaxy thus dominate the resulting shape. At larger radii, greater differences between CDM and SIDM axis ratios are also expected according to DM-only models, but again the halo-to-halo variation in the assembly history of DM+Baryon causes larger differences in halo shape than the variation in σ/m does. In general, the flattening profile with radius tends to be concave-down (most spherical at intermediate radii) rather than concave-up (most spherical at small and large radii) as predicted by previous work.

Although we find that halo-to-halo variation is larger than variation due to different σ/m, a possible test for SIDM could lie in predictions of the difference between the shape of the stellar distribution and that of the total mass distribution, both of which can be constrained by different methods. The overall shape of the total distribution (inferred from dynamics) is dominated by the flattened stellar component inside the LCR and by the more spherical DM component outside the LCR. The radius of this transition occurs at radius of 90 per cent of stellar mass $r_{\star,\,90}$ for CDM+Baryon simulations, but increases with increasing σ/m and occurs at the LCR scattering radius d_1 for SIDM+Baryon simulations, as the response of the DM to the growing galaxy becomes more important. There are several promising possibilities for measuring this radius with new survey data in the MW, and perhaps in other galaxies, in the coming decade.

Our results at very small radius ($\lesssim 2$ kpc) are limited by the need for better DM particle resolution for the SIDM-only simulations particularly, since as predicted the self-interactions significantly heat the central halo and reduce the particle density, limiting our ability to measure the shape in this region with our Lagrangian approach to simulations. In the case of all DM+Baryon simulations, this limitation is mitigated by the presence of the central galaxy, which deepens the gravitational potential and boosts the DM density in nearly all cases. However, better resolution in the central part would enable us to better study the transport of energy and angular momentum between the stellar and DM components, which will be the subject of future work.

Finally, we note that the galaxies formed in SIDM haloes with baryonic feedback differ from those in CDM in mostly subtle ways, and are generally similar (and consistent with observations) in their large-scale properties such as mass and scale radius. Therefore, SIDM remains a valid possibility for new DM physics.

ACKNOWLEDGEMENTS

RS acknowledges support from National Aeronautics and Space Administration (NASA) grants 19-ATP19-0068 and HST-AR-15809 from the Space Telescope Science Institute (STScI), which is operated by AURA, Inc., under NASA contract NAS5-26555. MBK acknowledges support from National Science Foundation (NSF) CAREER award AST-1752913, NSF grant AST-1910346, NASA grant NNX17AG29G, and HST-AR-15006, HST-AR-15809, HST-GO-15658, HST-GO-15901, and HST-GO-15902 from STScI. AW received support from NASA through ATP grants 80NSSC18K1097 and 80NSSC20K0513; HST grants GO-14734, AR-15057, AR-15809, and GO-15902 from STScI; a Scialog Award from the Heising-Simons Foundation; and a Hellman Fellowship. AG is supported by the Harlan J. Smith postdoctoral fellowship. This research is part of the Frontera computing project at the Texas Advanced Computing Center (TACC). Frontera is made possible by NSF award OAC-1818253. Simulations in this project were run using Early Science Allocation 1923870, and analysed using computing resources supported by the Scientific Computing Core at the Flatiron Institute. This work used additional computational resources of the University of Texas at Austin and TACC, the NASA Advanced Supercomputing (NAS) Division and the NASA Center for Climate Simulation (NCCS), and the Extreme Science and Engineering Discovery Environment (XSEDE), which is supported by NSF grant number OCI-1053575.

DATA AVAILABILITY

The CDM+Baryon FIRE-2 simulations are publicly available (Wetzel et al. 2022) at https://flathub.flatironinstitute.org/fire. The data for all other simulations used in this work are currently proprietary to members of the FIRE collaboration. Please contact the authors if interested.

REFERENCES

Ackerman L., Buckley M. R., Carroll S. M., Kamionkowski M., 2009, Phys. Rev. D, 79, 023519
Ahmed S. H., Brooks A. M., Christensen C. R., 2017, MNRAS, 466, 3119
Ahn K., Shapiro P. R., 2005, MNRAS, 363, 1092
Allgood B., Flores R. A., Primack J. R., Kravtsov A. V., Wechsler R. H., Faltenbacher A., Bullock J. S., 2006, MNRAS, 367, 1781
Arkani-Hamed N., Finkbeiner D. P., Slatyer T. R., Weiner N., 2009, Phys. Rev. D, 79, 015014
Auge C. et al., 2020, AJ, 160, 18
Blitz L., Spergel D. N., 1991, ApJ, 370, 205
Bonaca A., Hogg D. W., 2018, ApJ, 867, 101
Bondarenko K., Sokolenko A., Boyarsky A., Robertson A., Harvey D., Revaz Y., 2021, J. Cosmology Astropart. Phys., 2021, 043
Bovy J., Bahmanyar A., Fritz T. K., Kallivayalil N., 2016, ApJ, 833, 31
Boylan-Kolchin M., Bullock J. S., Kaplinghat M., 2011, MNRAS, 415, L40
Boylan-Kolchin M., Bullock J. S., Kaplinghat M., 2012, MNRAS, 422, 1203
Brooks A. M., Kuhlen M., Zolotov A., Hooper D., 2013, ApJ, 765, 22
Brooks A. M., Zolotov A., 2014, ApJ, 786, 87
Bryan G. L., Norman M. L., 1998, ApJ, 495, 80
Bullock J. S., Boylan-Kolchin M., 2017, ARA&A, 55, 343
Butsky I. et al., 2016, MNRAS, 462, 663
Chan T. K., Kereš D., Oñorbe J., Hopkins P. F., Muratov A. L., Faucher-Giguère C. A., Quataert E., 2015, MNRAS, 454, 2981
Conn A. R. et al., 2013, ApJ, 766, 120
Correa C. A., 2021, MNRAS, 503, 920
Creasey P., Sameie O., Sales L. V., Yu H.-B., Vogelsberger M., Zavala J., 2017, MNRAS, 468, 2283
Das M., McGaugh S. S., Ianjamasimanana R., Schombert J., Dwarakanath K. S., 2020, ApJ, 889, 10
Das P., Sanders J. L., 2019, MNRAS, 484, 294
Debattista V. P., Roškar R., Valluri M., Quinn T., Moore B., Wadsley J., 2013, MNRAS, 434, 2971
Debattista V. P., Gonzalez O. A., Sand erson R. E., El-Badry K., Garrison-Kimmel S., Wetzel A., Faucher-Giguère C.-A., Hopkins P. F., 2019, MNRAS, 485, 5073
Despali G., Sparre M., Vegetti S., Vogelsberger M., Zavala J., Marinacci F., 2019, MNRAS, 484, 4563
Dubinski J., Carlberg R. G., 1991, ApJ, 378, 496
Dutton A. A., Macciò A. V., Frings J., Wang L., Stinson G. S., Penzo C., Kang X., 2016, MNRAS, 457, L74
El-Badry K., Wetzel A., Geha M., Hopkins P. F., Kereš D., Chan T. K., Faucher-Giguère C.-A., 2016, ApJ, 820, 131
El-Badry K. et al., 2018, MNRAS, 473, 1930
Elbert O. D., Bullock J. S., Kaplinghat M., Garrison-Kimmel S., Graus A. S., Rocha M., 2018, ApJ, 853, 109
Erkal D., Belokurov V. A., Parkin D. L., 2020, MNRAS, 498, 5574
Feng J. L., Kaplinghat M., Tu H., Yu H.-B., 2009, J. Cosmol. Astropart. Phys., 2009, 004
Franx M., Illingworth G., de Zeeuw T., 1991, ApJ, 383, 112
Fritz T. K., Battaglia G., Pawlowski M. S., Kallivayalil N., van der Marel R., Sohn S. T., Brook C., Besla G., 2018, A&A, 619, A103
Garrison-Kimmel S., Boylan-Kolchin M., Bullock J. S., Kirby E. N., 2014, MNRAS, 444, 222
Garrison-Kimmel S. et al., 2017, MNRAS, 471, 1709
Garrison-Kimmel S. et al., 2018, MNRAS, 481, 4133
Garrison-Kimmel S. et al., 2019, MNRAS, 487, 1380
Governato F. et al., 2012, MNRAS, 422, 1231
Hattori K., Valluri M., Vasiliev E., 2021, MNRAS, 508, 5468
Hayashi K., Ibe M., Kobayashi S., Nakayama Y., Shirai S., 2021, Phys. Rev. D, 103, 023017
Helmi A., 2004, ApJ, 610, L97
Hesp C., Helmi A., 2018, preprint (arXiv:1804.03670)
Hopkins P. F. et al., 2018, MNRAS, 480, 800
Ibata R., Lewis G. F., Irwin M., Totten E., Quinn T., 2001, ApJ, 551, 294
Ibata R. A. et al., 2013, Nature, 493, 62
Ibata R. A., Ibata N. G., Lewis G. F., Martin N. F., Conn A., Elahi P., Arias V., Fernando N., 2014, ApJ, 784, L6
Jin Y., Zhu L., Long R. J., Mao S., Wang L., van de Ven G., 2020, MNRAS, 491, 1690
Johnston K. V., Law D. R., Majewski S. R., 2005, ApJ, 619, 800
Kado-Fong E., Greene J. E., Huang S., Beaton R., Goulding A. D., Komiyama Y., 2020, ApJ, 900, 163
Kamada A., Kaplinghat M., Pace A. B., Yu H.-B., 2017, Phys. Rev. Lett., 119, 111102
Kaplinghat M., Keeley R. E., Linden T., Yu H.-B., 2014, Phys. Rev. Lett., 113, 021302
Kaplinghat M., Valli M., Yu H.-B., 2019, MNRAS, 490, 231
Kim J.-h. et al., 2014, ApJS, 210, 14
Klypin A., Kravtsov A. V., Valenzuela O., Prada F., 1999, ApJ, 522, 82
Koda J., Shapiro P. R., 2011, MNRAS, 415, 1125
Koposov S. E., Rix H.-W., Hogg D. W., 2010, ApJ, 712, 260
Kroupa P., Theis C., Boily C. M., 2005, A&A, 431, 517
Küpper A. H. W., Balbinot E., Bonaca A., Johnston K. V., Hogg D. W., Kroupa P., Santiago B. X., 2015, ApJ, 803, 80
Kuzio de Naray R., McGaugh S. S., de Blok W. J. G., 2008, ApJ, 676, 920
Law D. R., Majewski S. R., 2010, ApJ, 714, 229
Law D. R., Majewski S. R., Johnston K. V., 2009, ApJ, 703, L67
Li H., Mao S., Cappellari M., Graham M. T., Emsellem E., Long R. J., 2018, ApJ, 863, L19
Libeskind N. I., Frenk C. S., Cole S., Jenkins A., Helly J. C., 2009, MNRAS, 399, 550
Loeb A., Weiner N., 2011, Phys. Rev. Lett., 106, 171302
Loebman S. R. et al., 2014, ApJ, 794, 151
Lynden-Bell D., 1976, MNRAS, 174, 695

Malhan K., Ibata R. A., 2019, MNRAS, 486, 2995
Mashchenko S., Wadsley J., Couchman H. M. P., 2008, Science, 319, 174
Moore B., 1994, Nature, 370, 629
Moore B., Ghigna S., Governato F., Lake G., Quinn T., Stadel J., Tozzi P., 1999, ApJ, 524, L19
Müller O., Pawlowski M. S., Jerjen H., Lelli F., 2018, Science, 359, 534
Narayan C. A., Saha K., Jog C. J., 2005, A&A, 440, 523
Navarro J. F., Frenk C. S., White S. D. M., 1996, ApJ, 462, 563
Oh S.-H., de Blok W. J. G., Walter F., Brinks E., Kennicutt R.C.,, Jr, 2008, AJ, 136, 2761
Oh S.-H. et al., 2015, AJ, 149, 180
Olling R. P., Merrifield M. R., 2000, MNRAS, 311, 361
Oman K. A. et al., 2015, MNRAS, 452, 3650
Oñorbe J., Boylan-Kolchin M., Bullock J. S., Hopkins P. F., Kereš D., Faucher-Giguère C.-A., Quataert E., Murray N., 2015, MNRAS, 454, 2092
Palau C. G., Miralda-Escudé J., 2019, MNRAS, 488, 1535
Palau C. G., Miralda-Escudé J., 2021, MNRAS, 504, 2727
Pawlowski M. S., Kroupa P., 2020, MNRAS, 491, 3042
Pawlowski M. S., Pflamm-Altenburg J., Kroupa P., 2012, MNRAS, 423, 1109
Pearson S., Küpper A. H. W., Johnston K. V., Price-Whelan A. M., 2015, ApJ, 799, 28
Peñarrubia J., Pontzen A., Walker M. G., Koposov S. E., 2012, ApJ, 759, L42
Peter A. H. G., Rocha M., Bullock J. S., Kaplinghat M., 2013, MNRAS, 430, 105
Planck Collaboration, 2014, A&A, 571, A16
Pontzen A., Governato F., 2012, MNRAS, 421, 3464
Posti L., Helmi A., 2019, A&A, 621, A56
Randall S. W., Markevitch M., Clowe D., Gonzalez A. H., Bradač M., 2008, ApJ, 679, 1173
Reino S., Rossi E. M., Sanderson R. E., Sellentin E., Helmi A., Koppelman H. H., Sharma S., 2021, MNRAS, 502, 4170
Ren T., Kwa A., Kaplinghat M., Yu H.-B., 2019, Phys. Rev. X, 9, 031020
Riley A. H., Strigari L. E., 2020, MNRAS, 494, 983
Robertson A., Harvey D., Massey R., Eke V., McCarthy I. G., Jauzac M., Li B., Schaye J., 2019, MNRAS, 488, 3646
Rocha M., Peter A. H. G., Bullock J. S., Kaplinghat M., Garrison-Kimmel S., Oñorbe J., Moustakas L. A., 2013, MNRAS, 430, 81
Sameie O., Creasey P., Yu H.-B., Sales L. V., Vogelsberger M., Zavala J., 2018, MNRAS, 479, 359
Sameie O., Benson A. J., Sales L. V., Yu H.-b., Moustakas L. A., Creasey P., 2019, ApJ, 874, 101
Sameie O., Chakrabarti S., Yu H.-B., Boylan-Kolchin M., Vogelsberger M., Zavala J., Hernquist L., 2020a, preprint (arXiv:2006.06681)
Sameie O., Yu H.-B., Sales L. V., Vogelsberger M., Zavala J., 2020b, Phys. Rev. Lett., 124, 141102
Sameie O. et al., 2021, MNRAS, 507, 720
Samuel J. et al., 2020, MNRAS, 491, 1471
Samuel J., Wetzel A., Chapman S., Tollerud E., Hopkins P. F., Boylan-Kolchin M., Bailin J., Faucher-Giguére C.-A., 2021, MNRAS, 504, 1379
Sanderson R. E. et al., 2018, ApJ, 869, 12
Sanderson R. E. et al., 2020, ApJS, 246, 6
Shao S., Cautun M., Frenk C. S., 2019, MNRAS, 488, 1166
Spergel D. N., Steinhardt P. J., 2000, Phys. Rev. Lett., 84, 3760
Tollet E. et al., 2016, MNRAS, 456, 3542
Tulin S., Yu H.-B., 2018, Phys. Rep., 730, 1
Tulin S., Yu H.-B., Zurek K. M., 2013, Phys. Rev. D, 87, 115007
Valli M., Yu H.-B., 2018, Nature Astronomy, 2, 907
Valluri M., Debattista V. P., Quinn T. R., Roškar R., Wadsley J., 2012, MNRAS, 419, 1951
Valluri M., Price-Whelan A. M., Snyder S. J., 2021, ApJ, 910, 150
Vasiliev E., Belokurov V., Erkal D., 2021, MNRAS, 501, 2279
Vera-Ciro C., Helmi A., 2013, ApJ, 773, L4
Vera-Ciro C. A., Sales L. V., Helmi A., Frenk C. S., Navarro J. F., Springel V., Vogelsberger M., White S. D. M., 2011, MNRAS, 416, 1377
Vogelsberger M., Zavala J., Loeb A., 2012, MNRAS, 423, 3740
Vogelsberger M., Zavala J., Cyr-Racine F.-Y., Pfrommer C., Bringmann T., Sigurdson K., 2016, MNRAS, 460, 1399
Walker M. G., Peñarrubia J., 2011, ApJ, 742, 20
Wegg C., Gerhard O., Bieth M., 2019, MNRAS, 485, 3296
Wetzel A. R., Hopkins P. F., Kim J.-h., Faucher-Giguère C.-A., Kereš D., Quataert E., 2016, ApJ, 827, L23
Wetzel A. et al., 2022, preprint (arXiv:2202.06969)
Yoshida N., Springel V., White S. D. M., Tormen G., 2000, ApJ, 544, L87
Zavala J., Vogelsberger M., Walker M. G., 2013, MNRAS, 431, L20

APPENDIX A: ELLIPSOIDAL VERSUS SPHERICAL SHELLS

As discussed in Section 4, we use the triaxial ellipsoidal shape profiles to calculate density and velocity profiles in ellipsoidal shells. However, past work has largely relied on spherical shells to calculate these profiles. Fig. A1 shows the difference in DM local collision rate $[\Gamma_{\rm scatter,\,E}(d) - \Gamma_{\rm scatter,\,S}(r)]/\Gamma_{\rm scatter,\,E}(d)$ between ellipsoidal shells and spherical shells, where $\Gamma_{\rm scatter,\,E}(d)$ and $\Gamma_{\rm scatter,\,S}(r)$ are the $\Gamma_{\rm scatter}$ for ellipsoidal and spherical methods, respectively. We note that the ellipsoidal shells have larger $\Gamma_{\rm scatter}$ due to having larger estimates of the DM density, particularly at larger d. This is the effect of 'smearing' across isodensity contours when using spherical shells to compute densities. The DM velocity profiles have negligible differences between the ellipsoidal and spherical methods, suggesting that the local velocity ellipsoid is relatively isotropic.

We calculate the difference in scattering radius when using ellipsoidal shells (d_1) rather than spherical shells (r_1) as $\Delta_1 = d_1 - r_1$, where $\Delta_1 = 2$ kpc for SIDM-only $\sigma/m = 10\ {\rm cm^2\,g^{-1}}$. For SIDM+Baryon $\sigma/m = 1$ and $10\ {\rm cm^2\,g^{-1}}$, the differences are $\Delta_1 = 0.6$–1.6 kpc and $\Delta_1 = 1.$–$2.$ kpc, respectively. The $\Delta_1 \sim 5$–20 per cent difference demonstrates the importance of using ellipsoidal shells fit

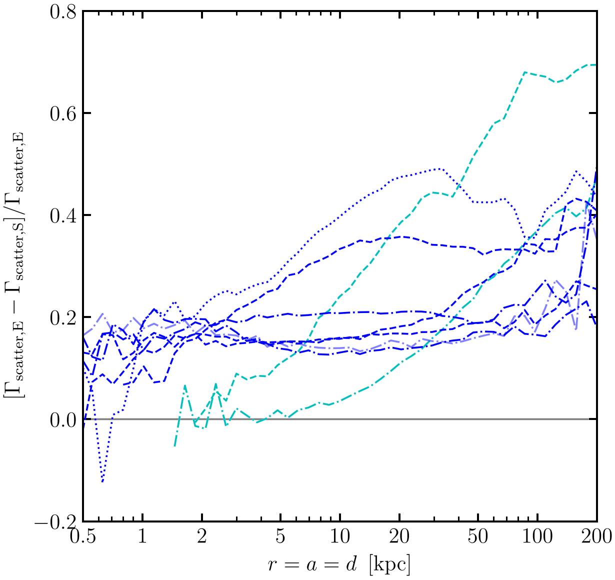

Figure A1. Difference in DM local collision rate of simulated MW-mass galaxies. The difference when averaging over shells of ellipsoidal distances d versus spherical radii $r = a$, $[\Gamma_{\rm scatter,\,E}(d) - \Gamma_{\rm scatter,\,S}(r)]/\Gamma_{\rm scatter,\,E}(d)$ (equation 6) as a function of $d = r = a$ for SIDM simulations. Shells are matched so that spherical radius r is equal to the semimajor axis a of the ellipsoid used to compute d. Line-styles and colours follow the legend in Fig. 4. Using ellipsoidal shells leads to larger $\Gamma_{\rm scatter}$, mostly because of an increase in the computed DM density. The difference in the local collision rate increases for the ellipsoidal shells method away from the centre of the galaxies.

to the isodensity contours to estimate density and velocity profiles. The use of ellipsoidal shells is even more important for the stars, gas, and total mass distributions, since these have less spherical shapes, and thus larger density and velocity differences between the two methods compared to the DM component.

APPENDIX B: GEOMETRICAL MEAN OF AXIS LENGTHS

Fig. B1 shows the axial ratio $s = c/a$ versus the geometrical mean of the axis ratios $R = (abc)^{1/3}$, instead of semimajor axis distance $r = a$ as in Fig. 8. This plot is included to facilitate comparison with previous work on halo shapes. The most important difference to note relative to Fig. 8 is that the axial ratio curves have shifted towards smaller radii, since the ellipsoidal geometrical mean radius R is always less than or equal to semimajor axis $r = a$ by definition. Due to the relatively spherical shape of the DM component, its curve is shifted the least, while the profile of the gas component, which is the most flattened, has shifted the most. Rapid changes in the flattening of neighbouring ellipsoids have the effect of producing non-functional curves, such as observed for the gas in `m12m` SIDM+Baryon $\sigma/m = 1\ \mathrm{cm}^2\ \mathrm{g}^{-1}$ near $R \sim 1$ kpc. This is a result of the fact that the definition of R does not guarantee that it must always increase with increasing ellipsoid semimajor axis $r = a$.

Similarly, Fig. B2 shows the triaxiality T versus the geometrical mean of the axis lengths R, instead of semimajor axis $r = a$. The plot shows a similar shift leftward for all the triaxiality curves, but the shift is less pronounced since the triaxiality depends on all three axis lengths a, b, and c. This shift does in general reduce the apparent prolateness of the CDM+Baryon and SIDM+Baryon

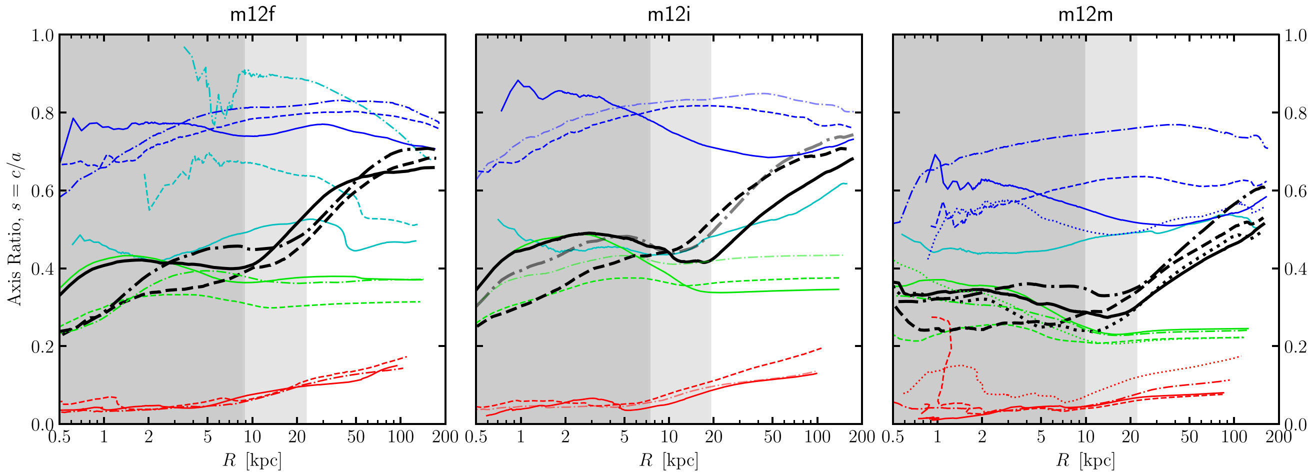

Figure B1. Shape profiles of simulated MW-mass galaxies as a function of R. Minor-to-major axial ratio $s = c/a$ as a function of geometrical mean radius R for different species (DM, stars, and gas) in three sets of MW-mass galaxy simulations: `m12f` (left), `m12i` (centre), and `m12m` (right). Line-styles, colours, and shaded areas follow the legend in Fig. 4. An alternate version of this plot using the semimajor axis $r = a$ can be found in the main body of the work in Fig. 8. The literature often plots axis ratios versus this geometrical mean of the axis lengths R, which is therefore given here for comparison purposes. We note that the main difference is in how the curves have shifted leftward towards smaller radii.

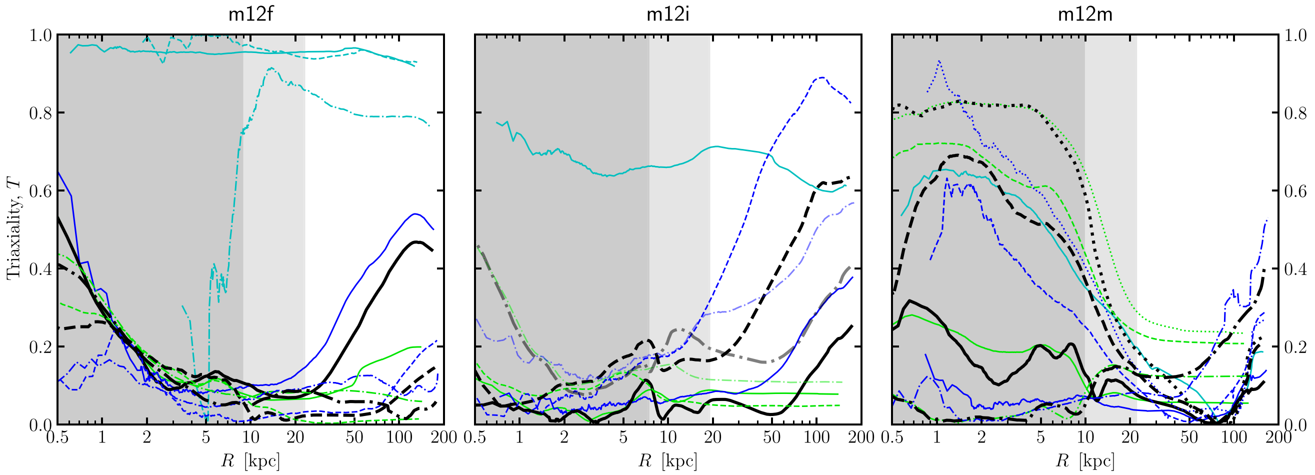

Figure B2. Triaxiality profiles of simulated MW-mass galaxies as a function of R. Triaxiality T as a function of geometrical mean radius R for different species (DM and stars) in three sets of MW-mass galaxy simulations: `m12f` (left), `m12i` (centre), and `m12m` (right). Line-styles, colours, and shaded areas follow the legend in Fig. 4. An alternate version of this plot using the semimajor axis $r = a$ can be found in the main body of the work in Fig. 9. The literature often plots triaxiality versus this geometrical mean of the axis lengths R, which is therefore given here for comparison purposes. We note that the main difference is in how the curves have shifted leftward towards smaller radii.

MW-mass galaxies at small radii, especially for `m12f` and `m12i`.

Overall, we consider that the use of semimajor axis length $r = a$ is preferable to the use of the geometrical mean of the axis lengths R, since observations of galaxies are 3D light and velocity (redshift) distributions projected as 2D light and velocity distributions on to the celestial sphere. Therefore, measuring a realistic R for any galaxy is a difficult and degenerate task. On the other hand, deprojecting *only* the semimajor and semiminor axis lengths of nested ellipsoids is a more feasible task, since measurements of the line-of-sight velocity distribution (e.g. Li et al. 2018; Jin et al. 2020) or stacked observations (e.g. Kado-Fong et al. 2020) can be used to constrain or marginalize over the inclination angle. This motivates the use of $r = a$, inside which density, velocity, and shape profiles of the baryons (and thus also DM) are then more easily estimated.

This paper has been typeset from a TEX/LATEX file prepared by the author.